

MoMuCAMS: A new modular platform for boundary layer aerosol and trace gas vertical measurements in extreme environments

Roman Pohorsky¹, Andrea Baccarini^{1,2}, Julie Tolu^{3,4}, Lenny H.E. Winkel^{3,4}, Julia Schmale¹

5 ¹Extreme Environments Research Laboratory, Ecole Polytechnique Fédérale de Lausanne, Sion, 1950, Switzerland

²Now at: Laboratory for Atmospheric Processes and their Impact, Ecole Polytechnique Fédérale de Lausanne, Lausanne, 1015, Switzerland

³Eawag, Swiss Federal Institute of Aquatic Science and Technology, Department of Water Resources and Drinking Water (W+T), Dübendorf, 8600, Switzerland

10 ⁴ETH Zurich, Swiss Federal Institute of Technology, Department of Environment Systems Sciences (D-USYS), Institute of Biogeochemistry and Pollutant Dynamics (IBP), Group of Inorganic Environmental Geochemistry, Universitätstrasse 16, 8092 Zurich, Switzerland

Correspondance to: Roman Pohorsky (roman.pohorsky@epfl.ch) and Julia Schmale (julia.schmale@epfl.ch)

Abstract

15 The Modular Multiplatform Compatible Air Measurement System (MoMuCAMS) is a newly developed in situ aerosol and trace gas measurement payload for lower atmospheric vertical profiling ~~in extreme environments~~. MoMuCAMS ~~is a multiplatform compatible system, has been~~ primarily designed to be attached to a helikite, a rugged tethered balloon type that is suitable for operations in cold and windy conditions. The system addresses the need for detailed vertical observations of atmospheric composition in the ~~boundary layer and lower free-troposphere, especially in polar and alpine regions. These regions are known to frequently experience strong temperature inversions, preventing vertical mixing of aerosols and trace gases, and therefore reducing the representativeness of ground-based measurements for the vertical column, causing a large informational gap.~~

20 The MoMuCAMS encompasses a box that houses instrumentation, a heated inlet, a board computer to stream transmit data to the ground for inflight decisions, and a power distribution system. The enclosure has an internal volume of roughly 100 L and can accommodate various combinations of instruments within its 20 kg weight limit (e.g. 20 kg for a 45 m³ balloon). This flexibility represents a unique feature, allowing the simultaneous study of multiple aerosol properties (number concentration, size distribution, ~~cluster ions~~, optical properties, chemical composition and morphology), as well as trace gases (e.g. CO, CO₂, O₃, N₂O) and meteorological variables (e.g., wind speed and direction, temperature, relative humidity, pressure). To the authors' knowledge, it is the first tethered balloon-based system equipped with instrumentation providing a full wide particle number size distribution for aerosol particles ~~starting within a large range, i.e. from 8 nm to 3370 nm~~, which is vital to understanding atmospheric processes of aerosols and their climate impacts through interaction with direct radiation and clouds. ~~MoMuCAMS has been deployed during two field campaigns in Swiss Alpine valleys in winter and fall 2021. It has been further deployed in Fairbanks, Alaska (USA) in January February 2022, as part of the ALPACA (Alaskan Layered Pollution and Chemical Analysis) campaign and in Pallas, Finland, in September October 2022, as part of the PaCE2022 (Pallas Cloud Experiment) study. The system flew successfully at temperatures of -36° C, in wind speeds above 15 m s⁻¹ and in clouds.~~

25 Here we present a full characterization of the specifically developed inlet system and novel, hitherto not yet characterized, instruments, most notably a miniaturized scanning electrical mobility spectrometer and a near-infrared carbon monoxide monitor.

30 ~~As of December 2022, the feasibility of MoMuCAMS has been tested during two field campaigns in the Swiss Alps in winter and fall 2021. It has been further deployed in Fairbanks, Alaska (USA) in January-February 2022, as part of the ALPACA (Alaskan Layered Pollution and Chemical Analysis) campaign and in Pallas, Finland, in September-October 2022, as part of the PaCE2022 (Pallas Cloud Experiment) study. Three cases from one of the Swiss Alpine studies are presented to illustrate~~

the various observational capabilities of MoMuCAMS ~~to perform high resolution measurements with different instrumental setups. Results from the first two case studies illustrate the breakup of a surface based inversion layer after sunrise and the dilution of a 50 to 70 m thick surface layer. The third case study illustrates the capability of the system to collect samples at a given altitude for offline chemical and microscopic analysis. We show two case studies with surface based inversions in the morning that allowed for observation of aerosol and trace gas dynamics in evolving boundary layer conditions. The vertical structure of the boundary layer featured in both cases a surface layer (SL) with a top between 50 and 70 m above ground level, dominated by traffic emissions leading to particle number concentrations up to seven times higher than in the residual layer above. Following sunrise, turbulent mixing led to rapid development of a mixed boundary layer and dilution of the SL within one to two hours. The third case study illustrates the capability of the system to perform aerosol sampling at a chosen altitude over several hours, long enough in low aerosol concentrations environments to perform chemical analyses. Trace elements were analyzed using inductively coupled plasma tandem mass spectrometry. The samples were also analyzed under a scanning electron microscope with energy dispersive x-ray and a transmission electron microscope to gain additional insights into their morphology and chemical composition. Such analyses are suitable to gain deeper insights into particles' origins, and their physical and chemical transformation in the atmosphere.~~

Overall, MoMuCAMS is an easily deployable tethered balloon payload with high flexibility, able to cope with the rough conditions of extreme environments. Compared to uncrewed aerial vehicles (drones) it allows to observe aerosol processes in detail over multiple hours providing insights on their vertical distribution and processes, e.g. in low level clouds, - that were difficult to obtain beforehand.

Introduction

One of the key challenges in aerosol science is understanding the large heterogeneity of particles in space and time. A particular gap exists in the knowledge of the vertical distribution and properties of aerosols since most detailed measurements are conducted at the surface. However, the vertical distribution of particles matters, in particular for their climatic effects (Carslaw, 65 2022). Aerosols interact directly with solar radiation by scattering and absorption, and indirectly as they influence the formation and properties of clouds (Boucher et al., 2013; Haywood and Boucher, 2000; Seinfeld and Pandis, 2016). In particular, subsets of particles, called cloud condensation nuclei (CCN) and ice nucleating particles (INP), can form liquid cloud droplets and ice crystals, respectively. For particles to affect clouds, they need to be transported to the height where clouds form. For the direct radiation interactions, the vertical location of absorbing aerosols matters specifically (Samset et al., 70 2013), because the absorbed energy causes local heating which stabilizes the temperature profile in the atmosphere with a variety of consequences such as cloud burn-off. Knowing the aerosols' vertical distribution can improve our estimates of aerosol radiative forcing, which is still the largest single contributor to uncertainty in anthropogenic radiative forcing (IPCC, 2021).

Understanding the vertical distribution becomes particularly important in environments, where the atmospheric boundary layer (ABL) is strongly stratified~~highly stable~~, such as in ~~the~~ Poles~~as~~ and alpine valleys~~mountainous~~ are two regions ~~were a stable boundary layer is commonly observed~~ (Chazette et al., 2005; Graversen et al., 2008; Harnisch et al., 2009; Persson et al., 2002). The stability~~ratification~~ leads to the layering of aerosols and reduced exchange processes, meaning that ground-based measurements are often not representative of cloud-level aerosol (Brock et al., 2011; Creamean et al., 2021; Jacob et al., 2010; McNaughton et al., 2011). Because the ABL represents an exchange interface between the surface and the free troposphere 80 (FT), it is highly relevant to study the different physical, chemical and dynamical processes that aerosol particles undergo in this lower part of the atmosphere (Jin et al., 2021; Kowol-Santen et al., 2001). Better constraining these processes will help determine to what extent aerosol particles will or will not be present at higher altitudes but also how particles will potentially mix down to the surface. The lack of observations strongly inhibits us from constraining numerical models, which do not

perform well in representing the vertical structure of aerosol properties (Koffi et al., 2016; Sand et al., 2017). ~~However, for assessing the direct and indirect radiative impact of aerosols knowing their vertical distribution is vital.~~

Remote sensing measurements from satellites or ground-based stations offer opportunities for large scale and/or continuous coverage. Nevertheless, remote sensing methods lack detailed information on particle composition and microphysics, and the temporal and spatial resolution is often too coarse for a detailed characterization of aerosol vertical processes (Gui et al., 2016; Mei et al., 2013). Furthermore, retrieval algorithms need validation and this can only be done with in situ measurements.

Shortcomings are particularly large in polar ~~and mountain~~ regions, where space-born aerosol-focused remote sensing (e.g., Cloud-Aerosol Lidar and Infrared Pathfinder Satellite Observation, CALIPSO) provides nearly no data north of 82°N, signals become attenuated under thick clouds, sensors are challenged by surface brightness, and aerosol concentrations are often too low (Kim et al., 2017; Mei et al., 2013; Thorsen & Fu, 2015). Ground-based remote sensing is limited in vertical resolution, because retrievals do not start at the surface but further aloft, which is a key problem in regions with very shallow ~~surface based temperature~~ inversions. In situ measurements from aircraft have provided valuable information (e.g. Pratt & Prather, 2010; Schmale et al., 2010, 2011), but they remain logically challenging, expensive, and sometimes cannot be carried out in complex and foggy terrain. Measurements at high speed can also cause flow-induced issues (Spanu et al., 2020) and do not allow for the observation of processes that unfold over minutes to hours such as mixing of ~~atmospheric~~ layers and cloud formation. Moreover, ~~typically an~~ aircraft ~~is typically limited in~~ for low altitude flights, especially under low visibility and ~~icing conditions. do not fly within the first hundreds of meters above the ground, missing therefore valuable information.~~

UAVs (uncrewed aerial vehicles) and tethered balloons are two effective alternative types of platforms for vertical in situ measurements of aerosol properties. UAVs offer advantages in terms of spatial coverage and flight pattern flexibility but are often limited in their lifting capacity and available space and weight for the payload. Tethered balloons represent a valuable alternative with better lifting capacities, extended flight duration (only limited by available power for instruments) and the ability to collect very high spatial resolution vertical profiles ~~in different weather conditions~~. Recently, there have been important developments in both ~~types of systems~~, UAVs and tethered balloons ~~instrumental platforms~~ (Bates et al., 2013; Ferrero et al., 2016; Mazzola et al., 2016; Pilz et al., 2022; Porter et al., 2020; Pasquier et al., 2022; Canut et al., 2016).

~~Focusing on tethered balloons, the HOVERCAT (Creamean et al., 2018) and the SHARK (Porter et al., 2020) have been developed to measure mainly INP. The AGAP (Mazzola et al., 2016) and the CAMP (Pilz et al., 2022) combine measurements of aerosol optical properties, aerosol number concentration and provide some information about particle size distribution, mainly based on optical particle counters. In addition, the AGAP also measures ozone (O₃) mixing ratios. This list is non-exhaustive and in addition, other tethered balloon systems have also been developed to study cloud microphysics and atmospheric turbulences (e.g. Canut et al., 2016; Pasquier et al., 2022). The systems platforms referenced above have typically been designed for specific targets and have therefore limited freedom in instrumental setup modification.~~

Here we present MoMuCAMS (Modular Multiplatform Compatible Air Measurement System), a new system for vertical measurements in the lower atmosphere that has been specifically designed with the aim to remain modular. It combines instruments for aerosol properties, trace gas and meteorological measurements, which can be combined in different configurations from one flight to another to provide a more comprehensive view on the various processes in the lower atmosphere. Additionally, ~~to the authors' best knowledge~~, MoMuCAMS is the first tethered balloon-based system providing a ~~widefull~~ particle ~~number~~ size distribution (P_{NSD}) from 8 to ~~33700~~ nm. Being able to identify the number concentrations and properties of particles in the CCN size range (> 100 nm) and in the optically most important size range, ~~~~~500 – 1000 nm, where the aerosol scattering efficiency is highest (Seinfeld and Pandis, 2016), is critical to reduce uncertainties in anthropogenic radiative forcing. ~~It should also be noted that in the specific context of Arcticpolar regions, CCN can be well below 100 nm in size~~ (Schmale et al., 2018; Karlsson et al., 2022). ~~The system addresses thus the need for measurements in the lower atmosphere in extreme environments with cold and windy conditions, where there is a particularly large informational gap. MoMuCAMS has been primarily designed to be attached under a helikite (Allsopp Helikite, UK). Helikites~~

~~are rugged and offer the advantage of gaining lift and remaining very stable under windy conditions, while most other tethered balloon systems typically cannot fly under such conditions. Our system can be operated by only two people and is light enough (<100 kg for the balloon setup, ~60 kg per winch and ~20 kg for the payload) to be deployed on sea ice.~~

130 ~~MoMuCAMS has been tested during two field campaigns in Swiss Alpine valleys in winter and fall 2021. It has been further deployed in Fairbanks, Alaska in January February 2022, as part of the ALPACA (Alaskan Layered Pollution and Chemical Analysis) (Simpson et al., 2019) field campaign and in Pallas, Finland, in September October 2022, as part of the PaCE2022 (Pallas Cloud Experiment) (Doulgeris et al., 2022) intensive field study.~~

135 This manuscript provides a ~~detailed~~ description and characterization of ~~the~~ MoMuCAMS system and ~~its~~ various instruments ~~under_in Sects.~~ 2 and 3. ~~Overall performances and Three~~ case studies ~~from MoMuCAMS deployments~~ are presented in Sect. 4 to demonstrate the system's ~~general~~ capabilities.

2 Technical description of payload and tethered balloon

2.1 MoMuCAMS payload characteristics

140 MoMuCAMS is a modular aerosol and trace gas measurement platform designed to be flown under a tethered balloon, while it can also be operated from other “tethers” (ropes) such as from cranes or alongside towers and tall buildings. The novelty of this platform lies in its flexibility to accommodate ~~a very large number of various~~ combinations of instruments within the weight and dimension limits. A list of instruments, which MoMuCAMS typically flies, is presented in Table 1. ~~Examples of different instrumental combinations respective scientific objectives are presented in Sect. 4. Importantly, MoMuCAMS is designed to accommodate guest instruments and~~ can easily be adapted for additional instruments.

145 The payload enclosure is a box with outer dimensions of 80 x 40 x 35 cm and a cone-shaped nose in the front (see Fig. 1). It provides a total inner volume of roughly 100 liters for instruments and batteries, which can be placed on two levels (“shelves”) or attached on the outside. The box is made of 30 mm thick extruded polystyrene plates. This material was selected for its low weight, rigidity and thermal insulation properties. Two aluminum T-elements placed at the front and back of the box support the enclosure from underneath and are used to attach it to the balloon. This system guarantees the stability of the payload in 150 the air. The box weighs (including the power distribution system and aluminum reinforcements) 3.2 kg. The instruments are powered by lithium-polymer (LiPo) batteries. ~~Batteries with a capacity between 9 and 22 Ah and a nominal voltage of 22.2 V are typically used. The maximum flight operation time will depend on the selected batteries, instrumental setup and ambient air temperature but usually ranges from two to ten hours.~~ The system is equipped with two 20 W resistive heaters connected to a thermostat to ensure the inner environment of the box remains above 0° C.

155 A custom-made data logging and communication system has been designed for MoMuCAMS. A Teensy 3.6 microcontroller programmed with Arduino IDE controls the different tasks. The microcontroller saves data from onboard sensors measuring internal temperature, barometric pressure, external and sampled air temperature and relative humidity, battery state of charge, particle number concentration from an optical particle counter and CO₂ mixing ratio. Data are also simultaneously ~~transmitted~~ ~~streamed~~ to the ground through an Xbee 3.0 radio module.

160 Figure 2 shows a schematic sketch of the inner design. ~~A subset of~~ ~~T~~he data is visualized live on a graphical interface, which helps for decision-making and sampling strategy adaptation during flights. Additionally, the operator can use the graphical interface to send commands to the MoMuCAMS microcontroller. ~~Commands include activation and filter position change of an 8-channel filter sampler for microscopy analysis (FILT), activation and flow control of a high flow stage impactor (HFI), activation of a relay to power additional instruments at a desired altitude and general shutdown of the system, to control various instruments remotely.~~

2.2 Helikite

A 45 cubic meter ~~Desert Star~~ helikite ([Desert star, Allsopp Helikites, GB](#)) from [Allsopp Helikites Ltd](#) is used to lift the payload.

170 The balloon consists of an outer shell and an inner membrane, which contains the helium. A helikite combines lifting capacity from the helium and from a kite, providing higher lift and good stability in windy conditions. The lifting capability of the helikite depends on the take-off altitude, i.e. atmospheric pressure, and wind speed. [The helikite used for this study has a volume of 45 m³, and a tether length of 800 m \(combined in two winches with 400 m of rope each\). It](#) ~~and~~ is [usually generally](#) sufficient to lift a payload between 12 and 20 kg. The helikite has been selected for its rugged characteristics, which allow for 175 deployments in the harsh environmental conditions of polar and mountain regions. The helikite/[MoMuCAMS setup](#) ~~haves~~ successfully flown at wind speeds up to 15 m s⁻¹, in temperatures down to -36° C, and in clouds [\(see Fig. S2, supplementary material\)](#). Note that when the air reaches very low temperatures (we estimate that -20° C represents a critical threshold), small punctures form in the balloon's inner membrane, which will consequently lead to helium losses over time and reduced 180 operation time (the inner membrane has to be repaired or replaced). [As wind increases, the zenith angle of the line increases as well, reducing the maximum altitude reachable with the helikite. The angle depends on the wind speed but also the net lift of the helikite, which will depend on the atmospheric pressure, inflation state of the balloon, presence of water, weight of the payload and tether. Estimates of zenith angles have been calculated from the horizontal displacement of the helikite \(measured by GPS\) and its altitude above ground level. Figure S3 \(supplementary material\) shows results for two fields campaigns. Generally, the zenith angle tends to stabilize between 45 to 50° at around 8 to 10 ms⁻¹. While in this manuscript we focus on the system built for a 45 m³ helikite with an 800 m long tether, MoMuCAMS is independent from the lifting platform and can be used with a larger balloon and longer tether to reach higher altitudes.](#)

3 Payload instrument characterization

In this section, we provide a detailed characterization of the inlet system (Sect. 3.1), and [present](#) instruments used on 190 ~~MoMuCAMS~~, which have not already been described in previous publications. In particular, we present the [advanced mixing condensation particle counter aMCPC \(aMCPC\)](#) (Sect. 3.2, [see Table 1 for abbreviation](#)), [miniaturized scanning electrical mobility sizer \(mSEMS\)](#) (Sect. 3.3) and Mira Pico gas analyzer (Sect. 3.65). The [printed optical particle spectrometer \(POPS\)](#) was described already by Gao et al. (2016) and Mei et al. (2020); nonetheless, we present here a characterization of our POPS 195 (Sect. 3.4) because it constitutes a reference instrument on the MoMuCAMS. Additionally, [setups for](#) filter based sample collection [and associated analytical techniques](#) for chemical composition [analysis](#) and electron microscopy are described in Sect. 3.76 and 3.87, respectively. Performance of a meteorological sensor (SmartTether, [AnaspHERE, USA](#)) is presented in Sect. 3.98. The reader is referred to Pikridas et al. (2019) and Pilz et al. (2022) for a description of the STAP (model 9406, Brechtel Manufacturing Inc., [USA](#)). [For the more commonly used ozone monitor \(model 205, 2BTech, USA\), the reader can refer to the Atmospheric Radiation Measurement \(ARM\) ozone handbook](#) (Springston et al., 2020) [and for an evaluation of flight performance of the carbon dioxide monitor \(GMP343, Vaisala, Finland\), the reader can refer to](#) Brus et al., (2021).

3.1. Inlet sampling efficiency and transmission losses

The inlet system is composed of a horizontal 30-cm long 3/8" stainless steel tube at the front of the box. Because the tethered balloon orients with the wind, the inlet is always facing into the wind direction. The tip of the inlet has a 30° downward bend 205 to prevent water droplets from entering. [Careful inspection of the inlet after each flight has not shown any signs of water infiltration in the sampling line.](#) A flexible thermofoil around the inlet heats the sample flow to reduce relative humidity to < 40 %, which corresponds to Global Atmosphere Watch standards (World Meteorological Organization, 2016), and prevents

ice formation when sampling in cold environments (see Fig. S2c). The inlet heating is controlled by a miniaturized thermostat (CT325, Minco) and set to be always above 0° C or ~10° C higher if ambient temperature is positive. Sample air temperature and relative humidity are monitored by a sensor (SHT80, Sensirion, CH). The sensor is placed inside the sampling line in parallel to the instruments to avoid particle losses. The sampled air is split into 1/4" branches and conductive black silicon tubing distributes the sampled air to the different instruments. Additionally, gas sensors such as the ozone monitor, and the stage impactor have their own inlet made of Teflon and Tygon, respectively. The carbon dioxide sensor is installed on the outside of the box and measures air flowing through passively.

The overall sampling performance of the main inlet has been characterized both experimentally and with the Particle Loss Calculator (PLC) (von der Weiden et al., 2009). Sampling efficiency (see Fig. 3) has been computed for wind speeds between 0 and 10 m s⁻¹, representative of most operating conditions, and a total sampling flow of 1.72 lpm, which is representative of a typical instrumental setup installed on MoMuCAMS. The flowrate may slightly vary from one setup to another. Results from the PLC indicate that oversampling, due to super-kinetic conditions, becomes important only for larger particles (> 2 µm) at higher wind speeds.

Transmission losses in the inlet have been experimentally tested with particles of different diameters (D_p). For particles up to 350 nm, polystyrene latex spheres (PSL) were nebulized and dried through a silica gel column (similar to the TSI 3062 type). The size selection was then refined with a Differential Mobility Analyzer (DMA). For particles larger than 350 nm, a Di-Ethyl-Hexyl-Sebacat (DEHS) solution was used to produce particles. After nebulization particles were dried and size selected with an aerodynamic aerosol classifier (AAC, Cambustion, UK). The aerodynamic diameter was later converted to mobility diameter for a more coherent comparison with the small particles selected with a DMA. A reference condensation particle counter (CPC) measured the particle number concentration after the DMA and AAC, while two CPCs were placed after the inlet. To represent the different tubing lengths inside the payload, one CPC was placed behind a short piece of black tubing (10 cm) and one was placed behind a longer piece (45 cm). The total flow through the main inlet was 1.72 lpm. Before the experiment, all CPCs were connected in parallel for direct comparison. Results from the CPC intercomparison are presented in Sect. 3.2.

Transmission losses in the inlet have been experimentally tested with polystyrene latex spheres (PSL) of different diameters (D_p). The nebulized PSLs were first dried through a silica gel column (similar to the TSI 3062 type) and the size selection was refined through a Differential Mobility Analyzer (DMA). A reference condensation particle counter (CPC) measured the particle number concentration after the DMA, while two CPCs were placed after the inlet. To represent the different tubing lengths inside the payload, one CPC was placed behind a short piece of black tubing (10 cm) and one was placed behind a longer piece (45 cm). The total flow through the main inlet was 1.72 lpm. Before the experiment, all CPCs were connected in parallel for direct comparison. Results from the CPC intercomparison are presented in Sect. 3.2.

Figure 3b shows the results of the inlet transmission test (colored dots with error bars) for ~~height~~six different PSL particles diameters and from the PLC for particles ranging from 8 to 37000 nm. Generally, results compare well between the experiment and the PLC with slightly lower losses for the shorter inlet. Transmission efficiency for particles between 50 and 1000 nm is very close to 100 % while smaller particles suffer from diffusional losses and larger particles from gravitational deposition. However, the losses are typically less than 10 %. Note that concentrations for PSLs with diameters of 510 and 995 nm were around 35 cm⁻³ and 20 cm⁻³, respectively. Therefore, small variation in the absolute concentration of one CPC might have had a large impact on the transmission efficiency calculation. This is probably the reason for the apparently large discrepancy with the short inlet measurement for 994 nm particles: the ~25 % difference is explained by just four or five particles cm⁻³ absolute difference (see bottom right purple dot on Fig. 3).

3.2 Advanced Mixing Condensation Particle Counter (aMCPC)

250 The compact advanced mixing condensation particle counter (aMCPC model 9403, Brechtel Manufacturing Inc., USA) is used for total particle number concentration measurements from 7 to 2000 nm, and weighs 1.7 kg. Two aMCPCs have been compared against a reference MCPC with the same measurement range (MCPC model 1720, Brechtel Manufacturing Inc., USA) with PSLs of D_p 150 nm. PSLs were nebulized and dried as described in Sect. 3.1. The two aMCPCs and the reference MCPC were connected in parallel behind the drier. Figure S44 in the supplementary material shows results of the 255 experiment. Both aMCPCs agree well (within 5%) with the reference MCPC.

In addition, ~~both aMCPCs' counting efficiency as a function of particle diameter was tested experimentally, the d_{50} cutoff (defined as the diameter where the counting efficiency reaches 50%) of both aMCPCs was tested experimentally by comparing the measured concentration of the aMCPCs and a reference ultrafine CPC (CPC3776, TSI, USA). All three CPCs were intercompared before the d_{50} cutoff measurements and concentration was corrected to account for differences in the counting efficiency (they all agree within a 7% factor). Particles were generated by nebulizing pure MilliQ water, which produces ultrafine particles due to small impurities inherently found in both the water and the container~~ (Knight and Petrucci, 2003; Park et al., 2012). ~~The particles were then dried and size selected with a DMA. The two aMCPCs and reference ultrafine CPC were then connected in parallel behind the DMA. The total aerosol flow was equal to 1.3 lpm, while the sheath flow in the DMA was set to 10 lpm. The tubing going to each CPC was of the same length to ensure similar losses (approximately 20 cm long). The size selection was done in steps of 0.5 nm from 5.5 to 10 nm with 600 s long measurements for each step. Results are shown on Fig. S5. Note that the automatic scanning sequence produced two measurements for 7 and 7.5 nm particles. For transparency, results of both measurements are shown separately on Fig. S5. The experimental results were fitted with an exponential function (Eq. 1)~~ (Stolzenburg and McMurry, 1991).

270
$$f(D_p) = A \left\{ 1 - \exp \left(\frac{B - D_p}{C - B} \ln(2) \right) \right\} \quad (1)$$

with fit results $A = 1.05$, $B = 5.13$ and $C = 6.01$ for aMCPC21 and $A = 1.02$, $B = 5.20$ and $C = 5.72$ for aMCPC22. The d_{50} cutoff (parameter C), defined as the diameter where the counting efficiency reaches 50%, was found to be equal to 5.76 and 5.76 nm for aMCPC 21 and 22, respectively. The detection efficiency for both aMCPCs reaches a plateau around 7 nm, in 275 agreement with the manufacturer's specifications. ~~Details are presented in the supplementary material (S1).~~

3.3 Miniaturized Scanning Electrical Mobility Sizer (mSEMS)

The miniaturized Scanning Electrical Mobility Sizer (mSEMS model 9404, Brechtel Manufacturing Inc., USA) is a compact particle size spectrometer providing particle number size distribution (PNSD) based on the mobility diameter for particles 280 between 8 and 300 nm. The instrument is composed of a soft X-ray aerosol charge neutralizer (Soft X-ray Charger XRC-05, HCTm CO. ltd., Korea), a miniaturized DMA (Differential Mobility Analyzer) column and an aMCPC with a total weight of 4.4 kg. The design of the DMA has been optimized to minimize the high voltage required for particle selection and therefore reduces problems of arching at higher relative humidity or lower pressure. The small internal volumes of the DMA and inlet tubing, and the fast aMCPC time response facilitate rapid scanning due to minimal smearing/mixing volumes inside the 285 instrument.

The performance of the mSEMS was tested with PSL with different particles covering its size range. Particles smaller than 50 nm were obtained by nebulizing pure MilliQ water using a portable aerosol generation system (PAGS, Handix scientific, USA). After nebulization, particles were dried through a silica gel dryer and size selected with a DMA. Particles larger than 50 nm were obtained by nebulizing PSL solutions and following the same procedure as with the pure MilliQ. For each size,

290 particles were nebulized for over 10 minutes to allow enough scans to be counted. The mSEMS was set to 60 bins at 1 second per bin. The mobility diameter (D_{mob}) was obtained by fitting a lognormal distribution to the measured PNSD and taking the peak value (mean). The uncertainty of the mean diameter was defined as one standard deviation of the fitted distribution. Results of the experiments are presented in Fig. 4a and Table 2. Overall, deviation in particle sizing, i.e. the relative difference between the particle size (D_p) and the measured distribution peak (D_{mob}) is below 7%. Maximum deviation of measured D_{mob} are 8% and 3.1% for 51 and 70 nm PSL, and below 1% for 150 and 240 nm PSL.

295 In addition, particle transmission through the neutralizer and DMA has been tested for different particlePSL sizes. For the experiment, PSL particles were nebulized and size selected with a first DMA. A standalone aMCPC was connected in parallel to the mSEMS after the first DMA. Transmission through the mSEMS (neutralizer + DMA) was calculated by comparing the particle number concentration measured by the two aMCPCs. Results are presented in Fig. 4b. A sinusoidal function (Eq. 24):

300

$$f(D_p) = \frac{A}{1+\exp(-B*(D_p-x_0))} \quad -(24)$$

305 with the following fit results $A = 1.00$, $B = 0.14$ and $x_0 = 13.46$, where x_0 is the 50% transmission point that was used to fit the experimental transmission results. Based on the measured losses below 30 nm, a correction is applied to the mSEMS data obtained in the field using Eq. (24). Figure 5 shows results of 10-minute averaged integrated particle number concentrations from the mSEMS against a standalone aMCPC measuring in parallel. Data was collected from a ground measurement station in Brigerbad, Switzerland between October 8 and October 11, 2021 (see Sect. 4.2 for campaign details). Figure 5a shows results for the original mSEMS data and Fig. 5b shows results after data correction. The color scale indicates the number concentration (N_{8-30}) of particles with D_{mob} between 8 and 30 nm to highlight the higher discrepancies between the mSEMS 310 and the aMCPC when the number of ultrafine particles increases. Dots indicating higher N_{8-30} are typically further away from the 1:1 line (Fig. 5a), confirming an underestimation of total number concentration because of ultrafine particle losses through the neutralizer and DMA. By applying the empirical transmission loss correction function, the slope of the linear regression increases from 0.61 to 0.79 and the scatter in the data is reduced (R^2 increases from 0.94 to 0.99, Fig. 5b). The remaining underestimation of the particle concentration can be explained by the narrower size range counted by the mSEMS (8 to 2870 315 nm) compared to the aMCPC (7 to 2000 nm). These measurements show that ultrafine particle losses in the mSEMS are non-negligible and a correction factor should be applied to improve measurement accuracy.

320 During flights, In this study, the instrument is operated with a 0.36 lpm sample flow and 2.5 lpm sheath flow. The We typically selected a size range is from 8 to 280 nm with 60 bins and a scan time of 1 minute (up scan). Note that the given values may need to be adjusted for environments with very low particle number concentrations (i.e. $< 100 \text{ cm}^{-3}$) to ensure good counting statistics, similarly to any electrical mobility sizer. Comparison of “up” versus “down” scan performance of the mSEMS has shown no significant difference between the two modes. Results of a 6-hour averaged PNSD for up and down scans is shown in Fig. S8. Given the lower time resolution of the mSEMS compared to other instruments onboard MoMuCAMS, a typical flight strategy consists in a fast ascending profile followed by a stepwise descent. Distance between each step varies according to the maximum altitude of the profile, desired time of flight and atmospheric conditions such as 325 temperature inversions or presence of stratified layers. A typical stop at a fixed altitude lasts at least five minutes to allow a minimum of five full scans for better counting statistics of the measured PSD. An example of such a flight pattern is presented in Sect. 4.2.

3.4 Portable Optical Particle Spectrometer (POPS)

330 The well-characterized Portable Optical Particle Spectrometer (POPS, Handix Scientific, USA) is used to obtain PNSD and number concentrations of particles between 186 and 33700 nm (Gao et al., 2016; Mei et al., 2020; Liu et al., 2021).

Sizing calibration of two POPS (1 for flights [POPS105] and 1 for ground measurements [POPS101]) were performed with polystyrene latex spheres (PSL) of sizes 240, 500, 800 and 994 nm. Nebulized particles passed inside a silica gel dryer to remove water. A 200-bin size segregation was used to improve the resolution of the size distribution around the main particle size mode. For each PSL diameter, the POPS measured for 5 minutes once the concentration became stable. Figure S6 shows results from measured optical diameters (D_{OPT}) calculated from lognormal fits of averaged PSDs. The uncertainty (error bars) is represented by one standard deviation of the fitted function. POPS105 shows deviations below 10% for PSLs up to 800 nm while POPS101 show slightly higher deviations up to 20% for 500 nm particles. Both POPS show higher deviation for 994 nm particles, i.e. 34 and 29% for POPS101 and 105, respectively. The higher deviation for particles around 1 μm can be explained by Mie resonance in this size range and has also been observed by Pilz et al. (2022). We follow therefore their recommendations by setting the POPS size resolution to 16 bins to minimize sizing errors.

Counting efficiency of the two POPS was tested against a reference Mixing Condensation Particle Counter (MCPC model 1720, Brechtel Manufacturing Inc). PSLs with a diameter of 230 nm were nebulized, dried and further size selected with a DMA. Background noise of the POPS was tested with particle-free air. Both POPS and the reference CPC showed concentration of 0 cm^{-3} . PSLs were then nebulized into the inlet. Concentrations were incrementally increased by modifying the particle-to-air ratio of the nebulizer. Figure S7 shows results of particle number concentrations of the two POPS against the reference CPC including all 16 bins (142 – 3370 nm, dots) and bins 4 to 16 (186 – 3370 nm, triangles). Results from Fig. S7 indicate that particles with diameters between 142 and 186 (bins 1 to 3) are wrongly detected by the POPS as total particle concentration increases. This phenomenon, potentially associated to stray light in the optics chamber, was already reported in previous literature (Gao et al., 2016; Mei et al., 2020; Pilz et al., 2022). According to the manufacturer, these wrong detections could also be explained by electronic noise from the detector, where fringes on the edge of the Gaussian signal are perceived as smaller particles by the software. It was therefore decided to only consider data for particles larger than 186 nm as the error induced by the first three bins is too high. Overall, both POPS shows very good agreement with the reference CPC with deviation below 10% for the total number concentrations.

Results are presented in the supplementary material (Fig. S3). POPS105 shows size deviations below 10% for PSLs up to 800 nm while POPS101 shows slightly higher deviations up to 20% for 500 nm particles. Both POPS show higher deviation for 994 nm particles: 34% and 29% for POPS 101 and 105, respectively. The higher deviation for particles around 1 μm can be explained by Mie resonance in this size range and has also been observed by Pilz et al. (2022). We follow therefore their recommendations by setting the POPS size resolution to 16 bins (instead of a higher number) to reduce sizing artefacts.

Based on counting efficiency tests (see details in the supplementary material, Fig. S4), it appeared that particles with diameters between 142 and 186 (bins 1 to 3) are wrongly detected by the POPS as total particle concentration increases. This phenomenon can be explained by electronic noise from the detector, where fringes on the edge of the Gaussian signal are perceived as smaller particles by the software. It was therefore decided to only consider data for particles larger than 186 nm as the error induced by the first three bins is too high. Overall, both POPS show very good agreement with the reference CPC with deviation below 10% for the total number concentrations.

365

3.5 Comparison of mSEMS and POPS

To assess the comparability of the mSEMS and POPS measurements, the instruments have been installed in parallel of a scanning electrical mobility spectrometer (SEMS Model 2100, Brechtel Manufacturing Inc., USA). The mSEMS and POPS were directly connected to the same whole air inlet as the SEMS. Figure 6 shows results of the comparison between January 30 and January 31, 2022. Panel (a) and (b) show comparative timeseries of 10 min averaged integrated total particle number concentration between the SEMS (blue) and mSEMS (red), and between the SEMS and POPS (green), respectively. The particle size range was from 8 to 270 nm (N_{8-270}) and 180 to 1500 ($N_{180-1500}$) for panel (a) and (b), respectively. Note that the

size range of each instrument differed slightly because of respective bin limits. Regression slopes of 0.98 and 0.89 confirmed good agreement between the instruments for particle number concentration in their respective size range. Figure 6c shows PNSD from the three instruments between 02:00 and 04:00 on January 31, 2022 (shaded area on Fig. 6a and b). The full line represents the median PNSD and the colored shading represents the interquartile range. Note that no conversion was made to transform the optical diameter from the POPS into the electrical mobility diameter. Given the different size ranges covered by the instruments and the several orders of magnitude of the y-axis, enlargements of the PNSD are shown in the corners of the figure to better assess the comparability of the instruments. To quantify the comparability of the measurements, both the mSEMS and SEMS PNSD were fitted with a lognormal distribution. The mode peaks of the mSEMS and SEMS are 29.7 and 33 nm, respectively; yielding a 10% difference. To compare size dependent particle counting between the mSEMS and the SEMS, the integrated particle concentration for several diameter intervals has been calculated. Results indicate that the mSEMS tend to overestimate the number of particles below 30 nm by 30 to 40 % compared to the SEMS. For particles larger than 30 nm, the agreement between the two instruments is well within 5 %. Detailed results for each size intervals is shown in Table S1 (supplementary material). Overall, the mSEMS and SEMS show very good agreement for total number concentration and show very comparative size distribution. For particles below 30 nm, the deviation is larger, which could potentially be attributed to difference of charging efficiency of the two neutralizers and slight differences in the inversion algorithm of the mSEMS and SEMS.

Comparison of normalized bin concentrations between the POPS and both electrical mobility analyzers showed correspondence within 5 % between the POPS and the mSEMS for the overlapping size range. Differences between the POPS and the SEMS is up to 20% but overall the overlapping of the optical and mobility diameters are within the uncertainty intervals (colored shading on Fig. 6c). Note that a full evaluation of a conversion from the POPS optical diameter to electrical mobility diameter would need to be performed to fully characterize the comparativeness of these instruments.

3.65 Mira Pico CO/N₂O/H₂O analyzer

The Pico (Mira Pico CO/N₂O, Aeris Technologies, USA) is a compact NDIR-based (non-dispersive infrared) gas analyzer. The instrument uses middle-infrared laser absorption spectroscopy to measure CO, N₂O dry mole fraction and H₂O with a sub ppb detection limit. Only a few studies have provided information on the performance of the Pico instrument, however only for the methane (CH₄) version (Commane et al., 2022; Travis et al., 2020). To the authors' best knowledge, this study provides a first experience of in flight operations is the first report on of the CO version.

The instrument is integrated inside a small Pelican case (L30 x W20 x H9 cm) and weighs 2.7 kg, including a battery with a 6-hour lifetime. The Pico can work in two different modes. The instrument is equipped with two programmable sampling ports. In its differential mode, the system switches between the two sampling ports at a user definable time interval (30 second by default). A catalytic CO-scrubber is placed in front of the first port, providing a zero measurement for each interval, effectively preventing any slow instrument drift. The software automatically removes the baseline (zero measurement) from the actual measurement. In this configuration, the Pico provides measurements at a 1-minute time resolution with a 1-ppb accuracy (the value is provided by the manufacturer but has not been validated experimentally). In its manual mode, the instrument samples only from one port with a 1-second time resolution. In this configuration, no baseline correction is applied to the measurements, reducing the overall accuracy. To estimate the reduction in precision due to unaccounted baseline drifts occurring over a typical flight period, we analyzed zero measurements (i.e., CO scrubber installed in front of sampling port and Pico operating in manual mode) for 90 minutes. We consider two standard deviations of the zero measurement distribution as an upper limit estimate of the measurement uncertainty in manual mode; this value is equal to 17 ppb.

For flight operation, the manual mode is preferred to provide the highest time resolution possible. To account for the baseline, the instrument is operated on the ground between flights in its differential mode. Before each flight, the instrument is placed

415 inside the box and brought outside until temperature inside the box has stabilized. The CO-scrubber is removed and the Pico
set to manual mode just before take-off. The baseline measurement for the last 3 hours before the flight and 3 hours after the
flight is then averaged and subtracted from the flight measurements. This operation should provide the best estimate for the
baseline deduction from the measured values. To identify, whether pressure or temperature changes have any influence on the
instrument's baseline, several flights were performed in differential mode. ~~No evident link between payload inner temperature,
420 ambient pressure and baseline variation was found, ultimately showing that baseline variability during and between flights was
similar (see Fig. 8b).~~ Figure 7a shows the baseline measurement for a full campaign with color codes indicating whether the
instrument was operated on the ground or in the air. Orange dots indicate that the instrument was operated inside a hut at
425 constant temperature of about 20° C, while blue dots are baseline measurements when the Pico was inside MoMuCAMS in
flight. Figure 7b shows in more detail the baseline variability on January 30, before, during and after a flight. The recorded
inner temperature of MoMuCAMS and atmospheric pressure are indicated to illustrate the lack of correlation between changing
environmental conditions and the instrument's baseline. Results indicate that the baseline remains stable over the campaign
and the flight does not affect the variability.

Note that during measurements, we recommend to save the high time resolution spectral files to control good data fitting or to
detect fitting issues. In case of fitting issues, the spectral files can be processed again to correct the data.

430 ~~So far~~ Although we demonstrate that vertical profiling does not affect the instrument's functionality, no quantitative
characterization of the Pico's performance is available besides the manufacturer's calibrations. A comparison with a reference
instrument or calibration gas should be done for future quantitative assessments of CO with the Pico.

435 3.76 Filter sampling for chemical analyses

In addition to online measurements, the MoMuCAMS system can also be equipped with instruments for offline analysis. Two
instruments are currently used to collect aerosol samples on filters for chemical and microscopic analyses. A more detailed
description of the instrumental setup, ~~types of analysis, filter preparation and handling, and analytical procedures~~ is given
below.

440 A high-flow multi-stage cascade impactor (HFI Model 131A, TSI, USA) is used to collect aerosol particles on filters. Each
stage ~~The is composed of~~ multiple nozzles, ~~pattern~~ achieving ~~ing~~ ~~cut~~ size selection similarly to the more common Micro-Orifice
Uniform-Deposit Impactors (MOUDI). A nominal sampling flow of 100 lpm is achieved by a radial flow impeller (Radial
blower U85HL-024KH-4, Micronel, CH) used in reverse as a lightweight pump as in Porter et al. (2020). The sampling flow
is constantly monitored by a flowmeter installed before the blower (SFM3000, Sensirion, CH). The HFI is equipped with 6
445 stages with the following cutoffs: 10, 2.5, 1.4, 1.0, 0.44 and 0.25 μm . Samples are collected for the 6 size cutoffs on 75 mm
diameter quartz fiber filters (QR-100, 0.38 mm thickness, Advantec MFS Inc., USA) and then on a 90 mm diameter quartz
fiber filters (AQFA, Merck Millipore Ltd, USA) to collect all particles below the lowest cutoff. ~~For airborne sampling, the
number of stages used is usually reduced to three to optimize mass collection on filters, especially if sampling time is reduced
because of flight duration restrictions imposed by regulations. A typical sampling strategy consists in bringing the tethered
balloon to a desired sampling altitude where it will hover. The blower can be activated and deactivated remotely and the flow
can be controlled.~~

For more detailed information on types of analysis, filter preparation and handling, and analytical procedures, the reader is
referred to the SI (Sect. S.5).

455 ~~Before sampling, all filters are baked for 6 hours at 550° C in separate aluminium pouches to reduce contaminants in the blanks
and directly sealed in plastic zip bags. We collect regular blanks for each sampling campaign. In particular, we have two types
of campaign blanks: regular blanks and field blanks. The former are brought to the field but not taken out from their aluminium~~

pouches (regular blank). The latter are installed in the filter sampler and retrieved shortly after to mimic field operations (field blank). After sampling, loaded filters are retrieved, folded in half and placed back in their respective pouches. Retrieval of filters is performed, if possible, at temperature conditions similar to sampling conditions to avoid any evaporation of volatile compounds. Filters are then stored at -20°C before analysis.

To quantify element concentrations in collected aerosols, half of the filters are first digested in a mixture of nitric acid (69% HNO₃, Suprapur; Roth), hydrogen peroxide (30% H₂O₂, for ultratrace analysis; Sigma Aldrich) and ultrapure water (18.2 MΩ cm; Nanopure Diamond™ system) using an MLS GmbH UltraCLAVE 4 microwave. Elements are then quantified in the digests using an Agilent 8900 inductively coupled plasma tandem mass spectrometry (ICP-MS/MS) (for a detailed description of the digestion and analysis, the reader is referred to the supplementary material, Sect. S3 and Table S1). The analysis of the blank filters is used to determine detection limits and whether field manipulation affects the background contamination of filters. Hereafter results of the background levels for Cu and Se are presented in Table 2 as a reference for the case study presented in Sect. 4.3. The resulting detection limits are calculated according to IUPAC recommendation (McNaught and Wilkinson, 1997), i.e., the mean plus three times the standard deviation of obtained blank concentrations. The background levels obtained for other trace elements and resulting detection limits are presented in the supplemental material (Sect. S3, Table S2). Results of regular and field blanks revealed no difference in the levels of trace elements, suggesting that the substrate itself and the digestion step are the largest sources of contaminations.

3.87 Filter sampling for Electron Microscopy

An 8-channel filter sampler (FILT Model 9401, Brechtel Manufacturing Inc., USA) is used to collect samples on substrates for electron microscopy analysis. Each channel holds a 13-mm Teflon Swinney filter holder. Polycarbonate filters with 0.4 µm pores (ref. number 321031, Milian Dutscher Group, CH) are used to collect particles for scanning electron microscopy with energy dispersive x-ray analysis (SEM/EDX). Polycarbonate filters offer a smooth surface and are mechanically rugged (Genga et al., 2018; Willis and Blanchard, 2002), which is ideal for particle observation and prevents deterioration of the substrate during sampling.

For Transmission Electron Microscopy (TEM) analysis, custom-made TEM grid holders were created to fit the standard 13-mm filter holders (see Fig. 8). Additionally, a “jetting” device (Brechtel Manufacturing Inc., USA), placed above the grid, reduces the inlet diameter and focuses the sampling beam onto the TEM grid. The real particle impaction efficiency has however not been characterized so far.

The filter sampler can operate between 0.5 and 3 lpm. However, the pump does not sustain a sampling flow above 1.8 lpm with the additional TEM grid holder and “jetting device”. Furthermore, higher sampling flows tend to destroy the grid’s carbon membrane. Therefore, we operated the FILT with a sampling flow of 1.5 lpm. Both the sample flow and the sampling stage can be remotely controlled from the ground. After filter retrieval, filters are stored at -20°C until analysis. Airborne sampling was first performed in October 2021, in a Swiss Alpine valley. Details electron microscopy analysis and Examples of collected aerosol particles with SEM/EDX and TEM are presented in Fig. 10. the supplementary material (Sect. S.6).

For scanning electron microscopy, the analysis is carried out on a Thermo Scientific Teneo. This machine is equipped with a Bruker XFlash EDX detector, as well as Everhart Thornley and Trinity (in column) electron detectors. Imaging and EDX spectroscopy are performed using a beam energy of 5 keV. A focused electron probe is scanned over a region of interest to collect EDX data in the form of spectrum images. For each region of interest, a second EDX map using a beam energy of 15 kV is acquired in case of ambiguity or peaks that overlap. To account for the signal from the sampling substrate, the beam is first focused on an aerosol free substrate area (red trace in Fig. 10). Before analysis, filters are coated with a 7 nm iridium layer to avoid charge accumulation at their surface. Two examples of particles collected during airborne filter sampling on September 28 and October 7, 2021 are shown on Fig. 10. EDX spectra for particle (a) shows traces of N, O, Fe and Si. Particle

500 (b) shows traces of N, Si, Al and K. Details on sample collection are presented in Sect. 4.3; however, a full analysis of SEM/EDX results is beyond the scope of this paper, which serves mainly as proof of concept for airborne aerosol sampling and subsequent microscopy analysis.

505 For transmission electron microscopy, the analysis is performed on a Thermo Scientific Teenai Spirit operating at an accelerating voltage of 120 kV. The images are acquired under bright field imaging conditions, in which only the directly transmitted beam, selected by the objective aperture, contributes to the image formation. TEM was performed on collected samples and confirmed that the system could effectively collect aerosol particles for TEM observations. An example of two particles collected during the September 28 flight is shown in Fig. S5. Similarly to the SEM/EDX example, these results are mainly presented for illustrative purposes of the system's capabilities for aerosol sampling and analysis and a more detailed interpretation is beyond the scope of this paper.

3.98 Meteorological measurements

510 Meteorological parameters including temperature (T), relative humidity (RH), barometric pressure (P), wind speed (WS) and direction (WD) are measured by a lightweight sonde (SmartTether, AnaspHERE, USA) placed below the payload. The SmartTether is contained in a compact plastic casing mounted on a carbon fiber arrow-shaped structure. A cup anemometer is placed at the front of the structure and a dart-like tail helps the sonde orient itself into the wind. Table 3 summarizes all measurements and the respective resolution, accuracy and operating range as provided by the manufacturer. During flight, data is transmitted to the ground and directly saved on the ground computer. Note that no data is saved locally and in case of communication loss, data is not saved. Furthermore, it appears that the SmartTether is sensitive to electromagnetic interferences and frequent loss of communication was experienced in some cases.

515 Two comparisons were performed on the ground between the SmartTether and a weather station equipped with a HygroVUE10 (Campbell Scientific) sensor, using an SHT35 sensing element (SHT35, Sensirion, CH). The first comparison was performed in Brigerbad, Switzerland on October 14, 2021. The second comparison was done in Fairbanks, Alaska on February 24, 2022.

520 During the first experiment, the SmartTether was attached to the tripod of the weather station at a height of 2 m (same height as the reference temperature sensor). During the second experiment, the SmartTether was attached to a small structure at 50 cm above the snow and about 2 m from the tripod because of restrained access to the tripod due to important snow depth.

525 During the second comparison, an additional T and RH sensor (SHT85, Sensirion, CH), used for the campaign, was placed near the SmartTether. Figure 9 shows the timeseries of T and RH for both experiments. Additionally, bottom panels show the incoming shortwave radiation flux (measured with an Apogee SN-500-SS). Data from the first comparison indicate that the SmartTether sonde is sensitive to solar radiation (Fig. 9a). In fact, the temperature sensor is directly exposed to the outside and no shield is present to block radiation. Our tests show that solar radiation leads to a temperature discrepancy of up to 4°C between the two shielded and unshielded sensors. This temperature discrepancy has a direct effect on the temperature dependent RH measurements.

530 Unfortunately, it is not trivial to evaluate how much the sensor is affected by radiation during flights because of the constant motion of the SmartTether. Furthermore, wind might also play a role on how the sensor is affected. Data show good agreement for temperature measurements when solar radiation is low as e.g., on October 13, 2021 after 17:45 and on February 24, 2022 (Fig. 9a and b). On February 24, RH values show a discrepancy up to about 4% (Fig. 9d). This discrepancy could be explained by higher uncertainties at high RH values. Looking at the SHT85 sensor, Fig. 9b and d show very good agreement with the reference sensor for T and RH.

535 Overall, the SmartTether provides reliable measurements when solar irradiance is low (overcast skies or at night) and/or wind speed is sufficiently high ($> 1 \text{ ms}^{-1}$) to maintain the sensor horizontal. In other cases, measurements can be biased and data should be treated accordingly. To address this issue, a solution including two sensors (SHT85, Sensirion, CH) in a shielding tube with active flow is under development in order to correct for the radiation sensitivity has been added to provide additional

540 redundant T and RH measurements. Figure S1 in the supplementary material shows the new radiation shield on the
MoMuCAMS box.

4 Field application

545 The performance of the MoMuCAMS prototype has been tested during two field campaigns in Swiss Alpine valleys in winter
and fall 2021. It has been further deployed in Fairbanks, USA in January-February 2022, as part of the ALPACA (Alaskan
Layered Pollution and Chemical Analysis) (Simpson et al., 2019) field campaign and in Pallas, Finland in September-October
2022, as part of the PaCE2022 (Pallas Cloud Experiment) (Doulgeris et al., 2022) intensive field study.

The following section discusses typical flight strategies of the measurement platform. Three case studies illustrating the
measurement capabilities of MoMuCAMS are then presented.

550 4.1 Sampling strategies and MoMuCAMS performance validation

555 Three flight patterns are typically applied with MoMuCAMS. The flight pattern depends on the instrumental setup and the
time resolution of the instruments data acquisition. Fast profiles consist in a continuous ascent followed by a continuous descent
and are performed to obtain a snapshot of the atmospheric column. Such a flight pattern is presented in a case study in Sect.
4.2.1. In this study, the velocity of the tether extension is 20 m per minute. The ascent and descent rate of the helikite depends
560 on the line angle but based on discussion from Sect. 2.2, can vary between 13 and 20 m per minute for a zenith angle of 50
and 0°, respectively. The spatial resolution for instruments recording at 1 Hz is therefore between 0.2 and 0.3 m. In the
configuration described in Sect. 3.3, the mSEMS has a vertical resolution between 13 and 20 m. For conditions with low
particle number concentrations, the scan time might need to be increased to improve counting statistics, reducing even further
its spatial resolution. Users will need to define the best combination of bin time and number of bins (size resolution) to optimize
the data quality and spatial resolution of the mSEMS.

565 Given the lower time resolution of the mSEMS compared to other instruments onboard MoMuCAMS, a second flight strategy
consists in a fast ascending profile followed by a stepwise descent. Stops allow the mSEMS to collect several scans at the
given altitude. The length of the stop at a fixed altitude depends on the total scan time of the mSEMS (one minute per scan in
this study) and should allow the mSEMS to measure several scans to improve counting statistic of the measured PNSD.
570 Ultimately, the distance between each steps and their respective duration vary according to the maximum altitude of the profile,
desired time of flight and atmospheric conditions such as temperature inversions or stratification. An example of such a flight
pattern is presented in a case study in Sect. 4.2.2.

575 For airborne sampling for offline analysis, the helikite is brought to a desired altitude (e.g. above the ABL or above a cloud,
depending on the research question). Once the helikite has reached the altitude, the filter samplers are activated remotely. For
airborne sampling with the HFI, the number of stages used is usually reduced from six to three to optimize mass collection on
filters, especially if sampling time is reduced because of flight duration restrictions imposed by regulations. The FILT typically
samples for 1 hour per channel. Sect. 4.2.3 shows results of two test flights for airborne sampling.

Altitude during flight is provided by the GPS of the SmartTether and is re-calculated during post processing of the data using
the barometric formula (Eq. 3),

$$h_b = \frac{T_0}{L_0} \ln\left(1 - \frac{p_b}{p_0}\right)^{\frac{L_0 R}{g}} \quad (3)$$

where, T_0 is the temperature at the surface, $L_0 = 6.5 \text{ K km}^{-1}$ is the mean environmental lapse rate, p_0 and p_b is the pressure at
the surface and balloon height, respectively, $R = 287 \text{ J kg}^{-1} \text{ K}^{-1}$ is the gas constant for dry air and g is the Earth's gravitational

acceleration. An uncertainty of ± 1 m for the altitude was calculated using the root mean square error for a 3-hour time series 580 of altitude measurement at a known altitude.

~~It is an integral part to the measurement strategy to the deviation is larger, which could potentially be attributed to difference of charging efficiency of the two neutralizers and slight differences in the inversion algorithm of the mSEMS and SEMS.~~

4.2 Case studies

585 From September 22 to October 14 2021, MoMuCAMS was deployed in a field campaign to study ~~and characterize~~ the vertical distribution of aerosols and trace gases in an Alpine valley in relation to the complex meteorological conditions of mountain regions. ~~13 flights were performed during the campaign and a total of 88 profiles were collected (ascending and descending profiles counted separately).~~ In addition to vertical profiling, ground-based measurements were performed to provide a continuous reference on the ground. A trailer with an inlet system was parked 30 meters from the helikite. Instruments from 590 the MoMuCAMS system sampled from the trailer between flights. Additionally, a SEMS measured P_{NSD} from 8 to 1100 nm and a weather station (Campbell Scientific, [USA](#)) measured meteorological parameters on the ground.

The study site was located in Brigerbad, Switzerland (46.29°N, 7.92°E), in the Rhône valley at an altitude of 653 m a.m.s.l. ~~At the site, the valley has an east west orientation and the valley floor is roughly 500 m wide. Heights of the nearest mountains to the north and south were 2900 and 2300 m, respectively.~~

595 Typical weather patterns exhibited diurnal temperature cycles during the whole period, ~~with an average temperature difference of 9.5° C between the 08:00 minimum and 16:00 maximum.~~

~~For interpretation purposes, time is given in local time, corresponding to Central European Summer Time (CEST or UTC+2).~~

In response to the radiation and temperature diurnal cycle, katabatic winds typically blew from the east between 22:00 and 600 09:00 with a mean velocity of 0.9 m·s⁻¹. ~~For interpretation purposes, time is given in local time, corresponding to Central European Summer Time (CEST or UTC+2).~~

The wind typically transitioned to a cross-valley southerly wind around 10:00 and further developed into a stronger westerly valley wind in the afternoon. The diurnal cycle was also characterized by surface temperature inversions occurring frequently during clear sky nights. ~~A rapid dissipation of the inversion layer typically followed after sunrise. This phenomenon was more marked during the second half of the campaign.~~

Several anthropogenic sources of atmospheric pollutants are located near the site, including industry, roads, private housing and agricultural fields. ~~Main contributing sectors to PM_{2.5} and BC have been estimated from the EMEP (European Monitoring~~

605 ~~and Evaluation Program) Centre on Emission Inventories and Projections gridded emission database (<http://www.emep-emissions.at/emission-data-webdab/>).~~ The percentage contributions by sector to annual emissions in 2020 for PM_{2.5} include stationary combustion (30.9%), industry (23.5%), off road vehicles (20%) and road transport (17.1%); and for BC stationary combustion (55.9%), road transport (22.2%) and off road vehicles (19.3%) as main contributors.

In the following section, we present case studies with three different instrumental setups illustrating the various measurement 610 capabilities of new insights on valley floor boundary layer processes that MoMuCAMS offers.

4.2.1 Case 1 – Evolution of aerosol and trace gas concentrations during a surface inversion dissipation

Six profiles (3 ascents and 3 descents) were measured on a cloud-free day on October 1st, 2021, from 08:50 to 12:30. ~~Table 4 615 summarizes the instrumental setup for these flights. The instrumental setup for this flight included a combination of trace gas monitors (CO, CO₂ and O₃) and aerosol instruments to measure the total number concentration (aMCPC) and PNSD above 186 nm (POPS). The combination of trace gas and aerosol measurements can be used to identify atmospheric layers with different emission sources based on ratios between the different tracers.~~

~~Figure S11a~~ ~~Figure 12a~~ shows the ground temperature (T), net radiation (NR) and wind speed (U) and direction evolution 620 from 08:00 to 12:45. At 09:30, the sun rose from behind the mountains, which led to a sharp increase in NR, followed by a

surface temperature increase. Winds at the surface remained low during the flights. Weak easterly katabatic winds were blowing until roughly 09:30 and then gradually developed into a cross-valley wind around 11:00. Above 50 meters, winds were slightly stronger (between 2 and 4.5 m·s⁻¹) and their east-northeast orientation remained rather constant through the flights (Fig. 11b and c). [Figure S11](#)[Figure 12b](#) and c show the ground-based measured PN_{SD} and integrated total concentration (black dots), rising from 08:00 and peaking between 09:00 and 09:30, followed by a gradual decrease until noon, which is consistent with the onset of convective mixing induced by surface warming. Figure 10d shows a time-series of the balloon altitude. The color of each altitude point indicates the particle number concentration [from 186 to 3370 nm \(N_{>186-3370}\) measured by](#) [from the POPS.](#)

Figures 11 and 12 show 4 different vertical profiles illustrating the evolution of the boundary layer. The selected profiles are indicated by numbers between brackets in Fig. 10d. Colors indicate the starting time of each profile. Figure 11a shows a [surface based](#) temperature inversion with a mean gradient of 1.8° C/100m during the first ascent starting at 08:55 (turquoise profile), indicative of a stable boundary layer (SBL) up to at least 250 m above ground level (AGL). The top of the inversion cannot be determined as the maximum reached altitude was still within the inversion layer. Figure 12 shows vertical profiles of particle number concentration and trace gas mixing ratios. The first profile shows a surface layer (SL) up to 50 m with increased [yet rather homogenous](#) concentrations compared to more elevated layers (>150 m). N₇₋₁₈₆ and N₁₈₆₋₃₃₇₀ concentrations were up to seven and two times higher than concentrations measured above 150 m, respectively. Ground-based measurements indicate that surface [particle number](#) concentrations started increasing around 08:00 (Fig. 10b) [with stable particle concentration before 08:00 \(not shown here\)](#). The increase at the surface is explained by the morning rush hour and reduced mixing volume due to valley walls and [SBL](#) [stable atmosphere](#), as has been observed previously in similar valley locations (Chazette et al., 2005 or Harnisch et al., 2009).

Between 80 and 125 m AGL, large peaks in the particle concentration and CO₂ mixing ratio were measured during the first ascent. These peaks were, however, not present on the following descent after 09:30 (Fig. 12, orange profile). At maximum peak intensity, the concentration of N₇₋₁₈₆ and N₁₈₆₋₃₃₇₀ was about three and four times larger than above 150 m, respectively. Compared to the SL, N₇₋₁₈₆ was 1.7 times lower at the plume altitude, but N₁₈₆₋₃₃₇₀ was two times larger. The CO₂ concentration shows an increase of 10% at the peak compared to surface values. CO exhibits only a weak signal at the same altitude. The exact origin of the plume is not known. The increase in CO₂ mixing ratio might suggest that the particles were recently emitted from an anthropogenic source. The different gas and particle ratios between the SL and the plume layer suggest different source contributions to the two layers. Given the altitude of the plume and the stability of the atmosphere, it can be hypothesized that the source was either located at the same altitude or was located at the surface and had higher injection height. The potential source could thus be either located on the valley slope or be a high stack from an industrial facility. It is not possible to say if the disappearance of the plume after the first flight was caused by the reduced atmospheric stability, which increased the dispersion and mixing of the plume, or by the termination of the emission process. This measurement provides however clear evidence that MoMuCAMS is effective in detecting plumes aloft and can be used to track emissions at higher elevations.

Not accounting for the above-discussed plume, concentrations in particles and gases decreased between 50 and 150 m (Fig. 12). [This negative gradient can be explained by a progressive reduction of the mechanical turbulent mixing caused by wind shear at the surface.](#)

[Wind shear arises from the difference between low winds in the decoupled SL and higher wind speed aloft \(Fig. 13b and c\).](#) [Mechanical turbulence induced by the shear would explain a slow diffusion of the different SL tracers into the adjacent layer.](#) [The diffusion rate remains small, and the SL appears to be decoupled from the rest of the atmosphere, allowing for the high concentration buildup, as observed.](#) Concentrations above 150 m show relatively homogenous profiles up to the maximum altitude with typically cleaner air. Given the atmosphere's stability during the first ascent, only a little or no vertical dispersion is occurring at these altitudes. Between the first ascent and the following descent, the surface temperature increased by 4.5° C in response to incoming solar radiation. The temperature of the entire column also increased, and the main surface-based

temperature inversion dissipated (11a). A shallow inversion layer of $1^{\circ}\text{C}/100\text{m}$ can still be observed in the second profile between 50 and 75 m (orange) and the third profile (purple) between 100 and 125 m. However, atmospheric stability generally decreases between the first and last profiles the surface temperature increases between the first and last profile, inducing convective mixing is induced turbulence and entrainment of air from the residual layer is entrained into the surface layer. This phenomenon can be observed in Fig. 10c and 12, where the high concentration at the surface in the first profile, indicated by the yellow colors, gradually decreased for each profile. The surface dilution is observed for all tracers, and by 670 11:00, all profiles appear rather homogenously distributed up to the maximum reached altitude. The efficient mixing effectively reduces particle and gas concentrations near the surface and alleviates air quality issues. The observed homogenous profiles suggest that the induced convective mixing and slope winds can transport polluted air from the surface to higher elevations, as previously reported by Furger et al. (2000) during the VOLTALP campaign in the Mesolcina valley in southern Switzerland. Similar conclusions were drawn by Ketterer et al. (2014) who reported an increase in local boundary layer height and transport 675 of aerosols from the valley bottom to the Jungfraujoch by slope winds. Aerosol particles can potentially be transported into the free atmosphere if the convective activity develops sufficiently, with subsequent further transport over longer distances in the FT. Contrary to Harnisch et al. (2009), who observed that slope winds could split at higher elevations in winter because of elevated shallow inversions and bring the transported pollution back to the center of the valley creating secondary pollution layers, we did not observe such a phenomenon. Results suggest that snow free slopes and stronger solar radiation in autumn 680 allow for effective upward transport of valley bottom pollution compared to winter.

4.2.2 Case 2 – Particle size distribution dynamics during the transition from a stable to a mixed boundary layer

Fourteen profiles (7 ascents and 7 descents) were performed on a cloud-free day on October 14, 2021, from 06:50 to 12:30. The instrumental setup of the flight is presented in Table 4. The instrumental setup for this flight included the mSEMS and the 685 POPS to analyze the difference in PNSD at various elevations in the presence of a surface based inversion and to investigate size dependent aerosol mixing during the breakup of the inversion layer.

Figure S12 Figure 15 shows measurements at the surface and the altitude profile timeseries of the helikite. The altitude profile (Fig. 13d) shows an alternation of fast ascending, descending, and stepwise profiles to allow the mSEMS to collect more scans. Stepwise profiles are typically performed during descents to increase sampling time at specific altitudes to run multiple scans 690 with the mSEMS to obtain several PSDs, which is important in low concentration environments, where single PSDs can be noisy. Based on the integrated particle number concentration (N_{8-280}) of the mSEMS (not shown here) and $N_{186-3370}$ (Fig. 13d, colored altitude profile dots) we distinguished three layers – a surface layer up to 70 m and a residual layer (RL) above 150 m. Similarly to the October 1 situation, a layer with a negative gradient of particle number concentration is observed between 70 and 150 m. This layer is referred hereafter as the intermediate layer (IL).

695 , an intermediate entrainment layer (EL) between 70 and 150 m with a negative particle concentration gradient, and an elevated layer above 150 m that we consider the residual boundary layer from the previous day, therefore, denoted as RL. A subset of collected temperature profiles, evenly spaced out and covering the whole flight period, has been selected to show the evolution of the atmospheric structure (Fig. 14). The numbered profiles are also indicated in Fig. 13d for more clarity.

Figure 14a shows the warming of the atmosphere following sunrise and the erosion of a surface based inversion. Figure 16a 700 shows a temperature inversion caused by nighttime surface radiative cooling (Fig. 15a). The positive temperature gradient up to the maximum reached altitude is indicative of stable boundary layer conditions. The SL and EL show gradients of $3.5^{\circ}\text{C}/100\text{m}$ and $0.6^{\circ}\text{C}/100\text{m}$, respectively. The temperature profile remained relatively stable until 09:45; after that, the entire column was warmed under the influence of solar radiation (Fig. 15a). Note that because of lower sun elevation and high surrounding mountain peaks, sunrise occurred roughly one hour later on October 14 than October 1.

705 Winds remained very low at the surface throughout the flights, with a slight dominance of easterly direction until sunrise. Wind direction then changed due to warming of southerly exposed slopes (Figure- S1245a). The vertical wind profile indicates increasing northeasterly winds with altitude during the first profiles. However, winds decreased after 10:45 and were almost nonexistent during the last profiles, indicative of a transitioning regime between katabatic and valley winds. Figure 13e shows the evolution of the SL. Despite the presence of a temperature inversion that developed overnight, the concentration in the 710 surface layer shows an evident increase after 07:15 (Figure. S1245c) in response to increased traffic emissions. We then observe a dilution and a larger vertical extent of the SL after 10:00. After 11:30, the surface layer is not visible anymore. Based on Fig. 13, Fig. 15e and d, three periods have been identified. The first period [P1] (07:30 – 09:59) represents the accumulation of pollutants at the surface in the SL. From 10:00 to 11:15 [P2], we observe a slightly greater vertical extent of the concentrated layer, indicative of a boundary layer development and increased ongoing vertical mixing. Finally, after 11:15 715 [P3], the surface layer is eroded and the entire vertical column profile is looks more homogenous, with no clear surface layer, consistent with the particle concentration decrease observed on Fig. 15e. Note that although the total particle concentration shows a decreasing trend shortly after 10:00, a peak of particles was measured around 10:40. This sudden burst was probably related to a very close source of anthropogenic emissions from a truck or gardening activities on the nearby parking lot. These nearby emissions might have biased to surface concentrations of the ascending profile at 10:47.

720 For each period, we investigated the P_{NSD} measured with the helikite to identify the main characteristics of each layer and see how they evolved with the development of the ABL. Results for P_{NSD} between 8 and 500 nm are presented in Fig. 15. The distribution was obtained by merging data from the mSEMS and the POPS. The two datasets present an overlap between 186 and 280 nm. Note that no conversion was made to transform the optical diameter from the POPS into the electrical mobility diameter. Left panels (a, c and e) show the color-coded evolution of the P_{NSD} in each layer. The SL is represented on the 725 lower panels for easier interpretation. Right panels (b, d and f) show the equivalent normalized distribution to better evaluate the relative contribution of different size modes to the P_{NSD}. Normalization was done by dividing dN/dlogDp values of each scan by the maximum dN/dlogDp measured for the respective scan, yielding a maximum value of 1 for the main peak. The SL (Fig. 15e and f) is characterized by the highest concentration during P1 (yellow) and P2 (light brown). Looking at the normalized distribution, the SL seems dominated by a small Aitken mode around 15 nm. A second mode is also visible during 730 P1 between 30 and 40 nm (small shoulder in the distribution). This second mode is also present on the upper layers and represents most likely aged particles emitted during the previous days. At P2, this larger Aitken mode is not visible anymore because of the stronger dominance of freshly emitted particles at the surface. Note the main peak at P2 (Fig. 15f) has shifted to the right compared to P1, indicative of potential growth of freshly emitted particles. Looking at the RL (Fig. 15a and b), the P_{NSD} exhibits a bimodal distribution with a main larger Aitken mode at 40 nm and an accumulation mode at roughly 150 nm. 735 This distribution seems to represent the background boundary layer composition of particles emitted from previous days (Aitken mode) and older particles that either remained suspended in the ABL for longer or were entrained from the free troposphere. At P1, the P_{NSD} also shows contributions from smaller nucleation mode particles. It can be hypothesized that emissions from cars and residential heating on the valley sides could directly contribute to this increase of smaller particles in the RL. The size distribution is, therefore, the result of the mixing between the aged mode from the previous day and fresh 740 emissions from higher up in the valley. At P2, the contribution of the nucleation mode is lower but with large variability, indicative of a transition to lower car traffic on the valley sides. A more systematic analysis under similar conditions would need to be performed to see if this phenomenon regularly occurs and better understand the underlying processes.

The IEL shows a similar feature to both the SL and RL. At P1, the P_{NSD} shows more similarity with the RL but with a less pronounced Aitken mode peak (Fig. 15c and d). At P2, the influence from the surface becomes clearer as the overall 745 concentration of nucleation and Aitken mode particles increases similarly to the SL. This indicates the onset of boundary layer growth and upward transport of surface emissions. At P3 (dark brown), the IEL and SL show very similar characteristics with the same concentration magnitudes for a nucleation mode peak, the larger Aitken mode (40 nm) and the accumulation mode

with overall lower total concentration indicative of a larger mixing volume due to increased boundary layer growthABL height. The observed increase in the nucleation mode contribution could be explained by a combination of NPF without growth and 750 direct emissions of ultrafine particles by cars. However, due to a limited amount of measurements in the layer, the actual source of the nucleation mode contribution remains uncertain. The RL shows similar features and concentration magnitudes as the lower layers for the Aitken and accumulation mode, but not for the nucleation mode, potentially indicating that these particles were only emitted later and did not have time to be transported higher up yet and where thus not captured. ~~The bimodal distribution observed in the former RL at P3 seems to constitute the background size distribution of the mixed boundary layer~~ 755 (ML) in the valley.

Overall, in the presence of a stable boundary layer, surface pollution is tightly linked to traffic emissions and is constrained in a shallow layer about 70 meters thick. This can lead to a rapid accumulation of pollutants. Ultrafine particles around 15 nm dominate the number concentration, which can be up to 5 times higher than the concentration of a mixed-boundary layer if we refer to the previous case study (Sect. 4.1). Particles that are not lost via coagulation or dry deposition remain in the boundary layer after the development of a ML and grow to a size of about 40 nm. ~~Part of these particles remain in the boundary layer after the development of a ML and grow to a size of about 40 nm.~~ These particles then constitute the boundary layer's particle background along with particles in the accumulation mode. The development of the ML in response to surface heating is fast, and the concentrated surface layer is typically diluted within 1 to 2 hours.

765 4.23.3 Examples of offline chemical analysis of airborne samples

Two test flights of airborne sample collection were performed on September 28 and October 7, 2021. For both flights, MoMuCAMS was equipped with the HFI for aerosol chemical analysis, 8-channel filter sampler (FILT) for SEM and TEM analysis, and the POPS. The flight pattern for both flights was similar. After reaching a desired sampling altitude, the HFI pump was turned on remotely while the balloon hovered at the same altitude. Simultaneously, the FILT sampled for roughly 770 1 hour per channel. As described in Sect. 4.1, the aim of airborne filter sampling is to reach layers decoupled from the surface. ~~The aim of the system is to sample air from layers that are decoupled from the surface to assess and compare the aerosol chemical composition to the mixed ABL or SL. Such a strategy can be applied to assess the chemical composition in decoupled layers above the surface when the lower troposphere is stratified.~~ However, given the vertical extent of the daytime mixed ABL during the field campaign and the tether length, sampling was performed in the mixed ABL and constituted mainly a 775 proof-of-concept of the sampling system. In both cases, the measured vertical profiles during ascent and descent indicated a well-mixed atmosphere with similar $N_{186-3370}$ concentrations throughout the entire column. The temperature profiles indicated an adiabatic lapse rate. An estimation of the aerosol mass concentration during sampling time was calculated from particle size distributionPNSD measurements from the POPS. The PNSD, was converted to a volume size distribution and integrated over all size bins to obtain the total volume concentration. The volume concentration was then converted to a mass concentration, 780 assuming a mean particle density of 1.6 g cm^{-3} , given the predominance of anthropogenic sources (Pitz et al., 2003). Flight 1 and 2 had average concentrations of $3.58 [1.43]$ and $1.48 [1.37] \mu\text{g m}^{-3}$, respectively. The values in brackets indicate the standard deviation of the measured mass concentration. Due to increased wind conditions (from $1.5 [2]$ to $9 [5] \text{ m s}^{-1}$ for flight 1 [2]) between the beginning and end of sampling, the altitude of the balloon decreased slightly. Table 4 provides details of both flights. Additionally, samples were also collected at the surface before flight 1 and, before and after flight 2 to obtain a 785 ground reference.

Collected aerosols have been analyzed for element concentrations (see supplementary material, Sect. S.73-6), and results for Cu and Se are presented here as an example. ~~High concentrations of Cu and Se in fine particles can have adverse health effects through direct inhalation or direct exposure via deposition (Daellenbach et al., 2020; De Santiago et al., 2014; Fang et al., 2017). Apart from being toxic at high concentrations, Se is an important micronutrient for humans (Winkel et al., 2015). It has~~

790 been estimated that up to 1 billion people worldwide have inadequate Se intakes, largely due to low concentrations in staple food crops (Combs, 2001). Because the atmosphere is an important reservoir of Se (estimated between 13,000 and 19,000 tons of Se per year; (Wen and Carignan, 2007)) supplying terrestrial ecosystems and food chains, it is essential to understand atmospheric Se cycling to predict atmospheric Se supplies to surface environments. Besides implications for human health, an important aspect of the Cu atmospheric cycle is the input of atmospheric Cu to aquatic systems (oceans), which can influence 795 primary productivity and phytoplankton community structure (Yang et al., 2019).

Figure 16 shows results of samples collected on the ground (a and c) and during flight (b and d). Ground sampling was performed with 6 stages and an after filter collecting all remaining particles below the lowest cutoff, while flights were performed with 3 stages only (0.44, 1 and 2.5 μm). Due to the low detection limit for Se, Se could be detected in almost all filters collected at the ground (between 12 to 18 h sampling time) and during flight (over 5 h). Due to higher Cu background 800 in filters and thus a higher detection limit, Cu could mainly be detected in filters collected at the ground. Only one Cu measurement in the 1 – 1.4 μm range was above detection limit for the aerosols collected during flight. The main limiting factor is the small aerosol mass concentrations obtained for the flight samples, which resulted in this case from a rather short low pumped sample flow and sampling time. Great care must thus be taken in future studies in term of sampling strategy 805 to ensure that the amount of collected material is sufficient for chemical analysis, especially in polar regions where mass concentration is typically much lower. –

Figure 18a b indicates that Se is mainly contained in submicrometer particles, with highest concentrations being measured in the 0.44 – 1 μm range. This result is consistent with one previous study looking at Se size distribution in aerosols collected at three sites in the Baltic sea (Dudzińska Huezuk & Bolalek, 2007). Interestingly, in contrast to Se, Cu concentrations increase with increasing particle size (Fig. 15e). Although it is out of the scope of this paper to investigate the factors controlling Cu and Se concentrations in the aerosol particles, the difference between Se and Cu size distribution could be explained by 810 different emission sources. Sources of Cu are typically metal industries, fossil fuel combustion, and abrasion of car breaking pads (Schauer et al., 2006; Yang et al., 2019). Vaporized copper sulfate used in the treatment of vineyards (Eckert and Jerochin, 1982) may also constitute a relevant source for the study area. For Se, 60 % of the atmospheric inputs have been estimated to be of natural origin and mainly from the biological production of volatile Se compounds, which are quickly oxidized and incorporated into the aerosol phase (Wen and Carignan, 2007). Despite the importance of the atmosphere in the biogeochemical 815 cycling of trace elements such as Cu and Se that are toxic or essential for humans and (micro)organisms, atmospheric data are still scarce, and often limited to point source sites, low temporal resolution (daily to weekly sampling), and/or one size fraction (PM2.5 or PM10). Our results show the feasibility of investigating aerosol composition with the adapted HFI on board of MoMuCAMS deployed at the ground or during flights. The MoMuCAMS system thus has great potential to improve our 820 understanding of aerosol sources and transport, which is of importance for various fields of environmental sciences including climate and trace element biogeochemistry.

54 Conclusions

This manuscript presents a newly developed system for tethered balloon observations of aerosols and trace gases in the lower atmosphere. MoMuCAMS is a modular measurement platform system, that allows different instrumental configurations to 825 combine observations of aerosol microphysical, optical and chemical properties with trace gas composition concentration measurements. To the authors' knowledge, this is the first time a tethered balloon system has been set up to measure a wide aerosol size distribution from 8 nm to 370 μm . This information allows us to better study the origin of aerosol particles, their physical and chemical transformation and transport at different altitudes in the lower troposphere relevant to the Earth's radiative budget. MoMuCAMS has been designed to be deployed with a helikite, because of the balloon's rugged 830 characteristics. It is ideal for flying in challenging extreme weather, including windy and cold and also low visibility

and icing conditions. Therefore, it can be used in Arctic or Antarctic regions, where many questions remain regarding aerosol-cloud interactions and aerosol radiative effects. The system has already proven to remain very stable at winds above 15 m s^{-1} and has flown at temperatures as low as -36°C .

Because MoMuCAMS uses several relatively new instruments, laboratory and field characterizations have been performed to demonstrate their ability to provide accurate measurements, high data quality and related uncertainties. The inlet system was also characterized for sampling efficiency and transmission losses to ensure a complete description of the system. Two portable aMCPCs showed deviation of particle number concentration below 5% from a reference MCPC. We tested the sizing accuracy and transmission losses of the mSEMS using PSLs of different sizes. The maximum deviations of measured mobility diameters were 8% and 3.1% for 51 and 70 nm PSL, respectively, and below 1% for 150 and 240 nm PSL. Based on the particle transmission tests, it is important to correct the mSEMS size distribution for losses of smaller particles. The manuscript provides a first empirical correction function. We characterized the aerosol transmission efficiency through the mSEMS (including neutralizer, DMA and tubing) and showed that it is important to correct the measured size distribution for losses of ultrafine particles. The manuscript provides a first empirical correction function that can be used for this purpose. Two POPS were tested for sizing and counting efficiency. Sizing accuracy remained between 10 and 20% up to 800 nm particles for the two instruments. To mitigate sizing errors for larger particles we decided to use a 16 bin size resolution (with 6 bins for particles larger than 800 nm). We also showed that the three smallest bins of the instrument are affected by spurious noise and should be excluded from the analysis, resulting in an effective cutoff size at 186 nm. The counting efficiency for particles larger than 186 nm for both POPS is within 10% from a reference CPC. No specific characterization was performed for the STAP, as it has already been well characterized for airborne observations (Bates et al., 2013; Pilz et al., 2022). The Mira Pico for CO measurements was presented and tests were performed to compare the instrument's performance in flight and on the ground characterized for its two modes of operation. No difference related to changes in environmental conditions (pressure and temperature) was observed in the instrument's baseline. The SmartTether weather probe was tested against a reference weather station. Results revealed that shielding of the sonde temperature sensor was insufficient and could lead to temperature and relative humidity biases. To address this, an additional temperature and relative humidity probe with better shielding and active flow has been added to provide more reliable measurements of T and RH.

Finally, procedures an instrumental setup for samples collection using a high flow impactor with a nominal flow of 100 lpm used for offline size segregated chemical analysis and a smaller 8-channel filter sampler for microscopic analysis of aerosol particles were presented. used for electron microscopy and chemical analysis using ICP MS/MS were presented. The analysis of chemical composition and aerosol morphology at higher altitudes will allow us to tackle questions related to aerosols' origins (e.g., anthropogenic versus natural), and their physical and chemical transformations in the atmosphere. A deeper understanding of the aerosols' composition, size and morphology will also allow a better constraining of their impact on climate and ecosystems. These results demonstrate the suitability of the instrumental set up for airborne in situ measurements. The reliability of MoMuCAMS has been tested during two field campaigns in the Swiss Alps, in January and September 2021 as well and it has been further deployed as in February 2022, in Fairbanks, Alaska, to study the vertical dispersion of air pollution in a sub-Arctic urban area in winter (ALPACA field study) (Simpson et al., 2019), and in September 2022, in Pallas, Finland, to study cloud formation (PaCE2022 field study) (Doulgeris et al., 2022). Three case studies from the September field campaign in 2021 in Brigerbad, in the Rhône valley, Switzerland featuring different instrumental setups have been presented in Sect. 4 to illustrate different observational capabilities of MoMuCAMS and their suitability for airborne in situ measurements. Case studies from October 1 and October 14, 2021, showed a surface-based inversion in the morning providing an opportunity to test the ability of MoMuCAMS to observe aerosol and trace gas dynamics in evolving boundary layer conditions. The vertical structure of the ABL in the morning featured in both cases a surface layer with a top between 50 and 70 m above ground level, an entrainment layer characterized by a negative gradient of pollutant concentration up to 150 m and a residual layer above. The surface layer build up typically occurred during morning rush hours and was dominated by traffic

emissions with a main particle size distribution mode around 15 nm. Total particle number concentrations (>7 nm) were up to seven times higher in the surface layer compared to the residual layer. We also observed an increase in ultrafine particles in the residual layer before the inversion breakup suggesting that traffic on the valley slopes constitutes a significant emission source into the residual layer in the early morning hours. Following sunrise, the surface layer typically dissipated within less than two hours leading to efficient mixing in the ABL and homogenous vertical distributions of particles and trace gases. Additionally, the first case study featured an elevated narrow pollution plume between 80 and 125 m above ground level on the first ascent.

A third case study illustrated the capability of the system to perform aerosol sampling at a chosen altitude over several hours. The ability of the system to sample for long periods has shown to be beneficial especially in conditions of low concentrations, where extended sampling is required to collect enough mass for chemical analysis. Collected samples can be used to provide size segregated chemical composition using mass spectrometry and/or SEM/EDX or TEM/EDX. The analysis of chemical composition and aerosol morphology at higher altitudes will allow us to tackle questions related to aerosols' origins (e.g., anthropogenic versus natural), and their physical and chemical transformations in the atmosphere. A deeper understanding of the aerosols' composition, size and morphology will also allow a better constraining of their impact on climate and ecosystems.

The [MoMuCAMS system](#)-characterization presented here provides a reference for future studies [and assures the reliability of the measurements](#) performed with MoMuCAMS. The case studies show the potential of our platform for vertical measurements of aerosol sources and processes in the lower part of the troposphere. The system can be continuously developed to integrate different instruments and to relate the in situ vertical observations with ground-based remote sensing (e.g., with an aerosol lidar) or drones carrying a subset of instruments for a more complete characterization of the ABL's horizontal and vertical structure.

Overall, MoMuCAMS is an easily deployable tethered balloon system able to cope with high wind speeds and cold conditions and to fly inside clouds, [providing reliable and high signal to noise data](#)[providing valuable in situ data in different boundary layer and weather conditions](#). Its ability to cope with harsh environmental conditions combined with the presented suite of instruments will contribute to providing new insights in the vertical distribution of aerosol and trace gases in the lower atmosphere.

The advantage of the MoMuCAMS helikite system over other airborne platforms is the ability to observe processes in situ over several hours without needing to move position, thereby providing insights that were difficult to obtain beforehand.

905 Code availability

The scripts used for the analysis in this study can be provided by contacting Roman Pohorsky (roman.pohorsky@epfl.ch).

Data availability

Data are freely available by contacting Roman Pohorsky (roman.pohorsky@epfl.ch).

Author contributions

910 JS conceived the original MoMuCAMS idea and obtained the funding. RP, AB and JS developed the MoMuCAMS system, performed the different laboratory and field measurements. JT and LW developed the analytical methodology for ICP-MS/MS

chemical analyses. RP and AB performed data analyses. RP wrote the manuscript with contributions from AB, JT and JS. All the authors commented on the manuscript.

Competing interests

915 The authors declare that they have no conflict of interest.

Acknowledgment

This work received funding from the Swiss Polar Institute (Technigrant 2019) and the Swiss National Science Foundation (grant no. 200021_212101). JS holds the Ingvar Kamprad Chair for Extreme Environments Research sponsored by Ferring Pharmaceuticals. The authors would like to acknowledge the work of Stéphane Voeffrey, Robin Délèze and Dennis Ellersiek 920 for their contribution to the MoMuCAMS construction and Emad Oveis for his assistance with the analysis of collected samples with the electron microscopes. We would like to thank Elyssa Beyrouti and Mike Chan from Eawag for their support with the sample preparation for the elemental analysis. We are very grateful to Martin Gysel and Barbara Bertozzi for letting us use their laboratory and for their precious time. We also would like to thank the Extreme Environments Research Laboratory 925 team for logistical and field experiment support. We highly appreciate the constructive feedbacks of the three anonymous referees for improvements of the manuscript.

References

930 Bates, T. S., Quinn, P. K., Johnson, J. E., Corless, A., Brechtel, F. J., Stalin, S. E., Meinig, C., and Burkhardt, J. F.: Measurements of atmospheric aerosol vertical distributions above Svalbard, Norway, using unmanned aerial systems (UAS), *Atmos. Meas. Tech.*, 6, 2115–2120, <https://doi.org/10.5194/amt-6-2115-2013>, 2013.

935 Boucher, O., Randall, D., Artaxo, P., Bretherton, C., Feingold, G., Forster, P. M., Kerminen, V.-M., Kondo, Y., Liao, H., Lohmann, U., Rasch, P., Satheesh, S. K., Sherwood, S., Stevens, B., and Zhang, X. Y.: Clouds and Aerosols. In: *Climate Change 2013: The Physical Science Basis. Contribution of Working Group I to the Fifth Assessment Report of the Intergovernmental Panel on Climate Change* [Stocker, T.F., D. Qin, G.-K. Plattner, M. Tignor, S.K. Allen, J. Boschung, A. Nauels, Y. Xia, V. Bex and P.M. Midgley (eds.)], 2013.

940 Brock, C. A., Cozic, J., Bahreini, R., Froyd, K. D., Middlebrook, A. M., McComiskey, A., Brioude, J., Cooper, O. R., Stohl, A., Aikin, K. C., de Gouw, J. A., Fahey, D. W., Ferrare, R. A., Gao, R.-S., Gore, W., Holloway, J. S., Hübner, G., Jefferson, A., Lack, D. A., Lance, S., Moore, R. H., Murphy, D. M., Nenes, A., Novelli, P. C., Nowak, J. B., Ogren, J. A., Peischl, J., Pierce, R. B., Pilewskie, P., Quinn, P. K., Ryerson, T. B., Schmidt, K. S., Schwarz, J. P., Sodemann, H., Spackman, J. R., Stark, H., Thomson, D. S., Thornberry, T., Veres, P., Watts, L. A., Warneke, C., and Wollny, A. G.: Characteristics, sources, and transport of aerosols measured in spring 2008 during the aerosol, radiation, and cloud processes affecting Arctic Climate (ARCPAC) Project, *Atmos. Chem. Phys.*, 11, 2423–2453, <https://doi.org/10.5194/acp-11-2423-2011>, 2011.

945 Brus, D., Gustafsson, J., Vakkari, V., Kemppinen, O., de Boer, G., and Hirsikko, A.: Measurement report: Properties of aerosol and gases in the vertical profile during the LAPSE-RATE campaign, *Atmos. Chem. Phys.*, 21, 517–533, <https://doi.org/10.5194/acp-21-517-2021>, 2021.

950 Canut, G., Couvreux, F., Lothon, M., Legain, D., Piguet, B., Lampert, A., Maurel, W., and Moulin, E.: Turbulence fluxes and variances measured with a sonic anemometer mounted on a tethered balloon, *Atmos. Meas. Tech.*, 9, 4375–4386, <https://doi.org/10.5194/amt-9-4375-2016>, 2016.

Carslaw, K. S.: Chapter 2 - Aerosol in the climate system, in: *Aerosols and Climate*, 9–52, 2022.

Chazette, P., Couvert, P., Randriamiarisoa, H., Sanak, J., Bonsang, B., Moral, P., Berthier, S., Salanave, S., and Toussaint, F.: Three-dimensional survey of pollution during winter in French Alps valleys, *Atmos. Environ.*, 39, 1035–1047, <https://doi.org/10.1016/j.atmosenv.2004.10.014>, 2005.

955 Commane, R., Hallward-Driemeier, A., and Murray, L. T.: Intercomparison of commercial analyzers for atmospheric ethane and methane observations, *Atmos. Meas. Tech. Disc.*, 1–13, <https://doi.org/10.5194/amt-2022-272>, 2022.

Creamean, J. M., de Boer, G., Telg, H., Mei, F., Dexheimer, D., Shupe, M. D., Solomon, A., and McComiskey, A.: Assessing the vertical structure of Arctic aerosols using balloon-borne measurements, *Atmos. Chem. Phys.*, 21, 1737–1757, <https://doi.org/10.5194/acp-21-1737-2021>, 2021.

960 Doulgeris, K. M., Lihavainen, H., Hyvärinen, A.-P., Kerminen, V.-M., and Brus, D.: An extensive data set for in situ microphysical characterization of low-level clouds in a Finnish sub-Arctic site, *Earth Syst. Sci. Data*, 14, 637–649, <https://doi.org/10.5194/essd-14-637-2022>, 2022.

965 Ferrero, L., Cappelletti, D., Busetto, M., Mazzola, M., Lupi, A., Lanconelli, C., Becagli, S., Traversi, R., Caiazzo, L., Giardi, F., Moroni, B., Crocchianti, S., Fierz, M., Močnik, G., Sangiorgi, G., Perrone, M. G., Maturilli, M., Vitale, V., Udisti, R., and Bolzacchini, E.: Vertical profiles of aerosol and black carbon in the Arctic: a seasonalphenomenology along 2 years (2011–2012) of field campaigns, *Atmos. Chem. Phys.*, 16, 12601–12629, <https://doi.org/10.5194/acp-16-12601-2016>, 2016.

Furges, M., Dommen, J., Gruber, W. K., Poggio, L., Pre, S. H., Gomiscek, B., Neininger, B., and Wotawa, G.: The VOTALP Mesolcina Valley Campaign 1996 - concept, background and some highlights, *Atmos. Environ.*, 34, 1395–1412, [https://doi.org/10.1016/S1352-2310\(99\)00377-5](https://doi.org/10.1016/S1352-2310(99)00377-5), 2000.

970 Gao, R. S., Telg, H., McLaughlin, R. J., Ciciora, S. J., Watts, L. A., Richardson, M. S., Schwarz, J. P., Perring, A. E., Thornberry, T. D., Rollins, A. W., Markovic, M. Z., Bates, T. S., Johnson, J. E., and Fahey, D. W.: A light-weight, high-sensitivity particle spectrometer for PM2.5 aerosol measurements, *Aerosol Sci. Tech.*, 50, 88–99, <https://doi.org/10.1080/02786826.2015.1131809>, 2016.

975 Genga, A., Siciliano, T., Siciliano, M., Aiello, D., and Tortorella, C.: Individual particle SEM-EDS analysis of atmospheric aerosols in rural, urban, and industrial sites of Central Italy, *Environ. Monit. Assess.*, 190, 456, <https://doi.org/10.1007/s10661-018-6826-9>, 2018.

Graversen, R. G., Mauritzen, T., Tjernström, M., Källén, E., and Svensson, G.: Vertical structure of recent Arctic warming, *Nature*, 451, 53–56, <https://doi.org/10.1038/nature06502>, 2008.

980 Gui, K., Che, H., Chen, Q., Yu, J., Zheng, Y., Lu, S., Wang, H., Wang, Y., Zhang, X., and Shi, G.: Analysis of the Error in Retrievals of Aerosol Optical Properties from Sunphotometer Measurements of CARSNET Due to a Variety of Objective Factors, *Atmosphere*, 7, 9, <https://doi.org/10.3390/atmos7010009>, 2016.

Harnisch, F., Gohm, A., Fix, A., Schnitzhofer, R., Hansel, A., and Neininger, B.: Spatial distribution of aerosols in the Inn Valley atmosphere during wintertime, *Meteorol. Atmos. Phys.*, 103, 223–235, <https://doi.org/10.1007/s00703-008-0318-3>, 2009.

985 Haywood, J. and Boucher, O.: Estimates of the direct and indirect radiative forcing due to tropospheric aerosols: A review, *Rev. Geophys.*, 38, 513–543, <https://doi.org/10.1029/1999RG000078>, 2000.

IPCC: Climate Change 2021: The Physical Science Basis. Contribution of Working Group I to the Sixth Assessment Report of the Intergovernmental Panel on Climate Change, , In Press, <https://doi.org/10.1017/9781009157896>, 2021.

990 Jacob, D. J., Crawford, J. H., Maring, H., Clarke, A. D., Dibb, J. E., Emmons, L. K., Ferrare, R. A., Hostetler, C. A., Russell, P. B., Singh, H. B., Thompson, A. M., Shaw, G. E., McCauley, E., Pederson, J. R., and Fisher, J. A.: The Arctic Research of the Composition of the Troposphere from Aircraft and Satellites (ARCTAS) mission: design, execution, and first results, *Atmos. Chem. Phys.*, 10, 5191–5212, <https://doi.org/10.5194/acp-10-5191-2010>, 2010.

995 Jin, X., Cai, X., Huang, Q., Wang, X., Song, Y., and Zhu, T.: Atmospheric Boundary Layer—Free Troposphere Air Exchange in the North China Plain and its Impact on PM2.5 Pollution, *J. Geophys. Res. Atmos.*, n/a, e2021JD034641, <https://doi.org/10.1029/2021JD034641>, 2021.

Karlsson, L., Baccarini, A., Duplessis, P., Baumgardner, D., Brooks, I. M., Chang, R. Y.-W., Dada, L., Dällenbach, K. R., Heikkinen, L., Krejci, R., Leaitch, W. R., Leck, C., Partridge, D. G., Salter, M. E., Wernli, H., Wheeler, M. J., Schmale, J., and Zieger, P.: Physical and Chemical Properties of Cloud Droplet Residuals and Aerosol Particles During the Arctic Ocean 2018 Expedition, *Journal of Geophysical Research: Atmospheres*, 127, e2021JD036383, <https://doi.org/10.1029/2021JD036383>, 2022.

Ketterer, C., Zieger, P., Bukowiecki, N., Collaud Coen, M., Maier, O., Ruffieux, D., and Weingartner, E.: Investigation of the Planetary Boundary Layer in the Swiss Alps Using Remote Sensing and In Situ Measurements, *Boundary-Layer Meteorol.*, 151, 317–334, <https://doi.org/10.1007/s10546-013-9897-8>, 2014.

1005 Kim, M.-H., Omar, A. H., Vaughan, M. A., Winker, D. M., Trepte, C. R., Hu, Y., Liu, Z., and Kim, S.-W.: Quantifying the low bias of CALIPSO's column aerosol optical depth due to undetected aerosol layers, *J. Geophys. Res. Atmos.*, 122, 1098–1113, <https://doi.org/10.1002/2016JD025797>, 2017.

Knight, M. and Petrucci, G. A.: Study of Residual Particle Concentrations Generated by the Ultrasonic Nebulization of Deionized Water Stored in Different Container Types, *Anal. Chem.*, 75, 4486–4492, <https://doi.org/10.1021/ac034355n>, 2003.

1010 Koffi, B., Schulz, M., Bréon, F.-M., Dentener, F., Steensen, B. M., Griesfeller, J., Winker, D., Balkanski, Y., Bauer, S. E., Bellouin, N., Berntsen, T., Bian, H., Chin, M., Diehl, T., Easter, R., Ghan, S., Hauglustaine, D. A., Iversen, T., Kirkevåg, A., Liu, X., Lohmann, U., Myhre, G., Rasch, P., Seland, Ø., Skeie, R. B., Steenrod, S. D., Stier, P., Tackett, J., Takemura, T., Tsigaridis, K., Vuolo, M. R., Yoon, J., and Zhang, K.: Evaluation of the aerosol vertical distribution in global aerosol models through comparison against CALIOP measurements: AeroCom phase II results, *J. Geophys. Res. Atmos.*, 121, 7254–7283, <https://doi.org/10.1002/2015JD024639>, 2016.

1015 Kowol-Santen, J., Beekmann, M., Schmitgen, S., and Dewey, K.: Tracer analysis of transport from the boundary layer to the free troposphere, *Geophys. Res. Lett.*, 28, 2907–2910, <https://doi.org/10.1029/2001GL012908>, 2001.

1020 Liu, Z., Osborne, M., Anderson, K., Shutler, J. D., Wilson, A., Langridge, J., Yim, S. H. L., Coe, H., Babu, S., Satheesh, S. K., Zuidema, P., Huang, T., Cheng, J. C. H., and Haywood, J.: Characterizing the performance of a POPS miniaturized optical particle counter when operated on a quadcopter drone, *Atmospheric Measurement Techniques*, 14, 6101–6118, <https://doi.org/10.5194/amt-14-6101-2021>, 2021.

Mazzola, M., Busetto, M., Ferrero, L., Viola, A. P., and Cappelletti, D.: AGAP: an atmospheric gondola for aerosol profiling, *Rend. Fis. Acc. Lincei*, 27, 105–113, <https://doi.org/10.1007/s12210-016-0514-x>, 2016.

1025 McNaughton, C. S., Clarke, A. D., Freitag, S., Kapustin, V. N., Kondo, Y., Moteki, N., Sahu, L., Takegawa, N., Schwarz, J. P., Spackman, J. R., Watts, L., Diskin, G., Podolske, J., Holloway, J. S., Wisthaler, A., Mikoviny, T., de Gouw, J., Warneke, C., Jimenez, J., Cubison, M., Howell, S. G., Middlebrook, A., Bahreini, R., Anderson, B. E., Winstead, E., Thornhill, K. L., Lack, D., Cozic, J., and Brock, C. A.: Absorbing aerosol in the troposphere of the Western Arctic during the 2008 ARCTAS/ARCPAC airborne field campaigns, *Atmos. Chem. Phys.*, 11, 7561–7582, <https://doi.org/10.5194/acp-11-7561-2011>, 2011.

1030 Mei, F., McMeeking, G., Pekour, M., Gao, R.-S., Kulkarni, G., China, S., Telg, H., Dexheimer, D., Tomlinson, J., and Schmid, B.: Performance Assessment of Portable Optical Particle Spectrometer (POPS), *Sensors*, 20, 22, <https://doi.org/10.3390/s20216294>, 2020.

Mei, L., Xue, Y., de Leeuw, G., von Hoyningen-Huene, W., Kokhanovsky, A. A., Istomina, L., Guang, J., and Burrows, J. P.: Aerosol optical depth retrieval in the Arctic region using MODIS data over snow, *Remote Sens. Environ.*, 128, 234–245, <https://doi.org/10.1016/j.rse.2012.10.009>, 2013.

1035 Park, J. Y., McMurry, P. H., and Park, K.: Production of Residue-Free Nanoparticles by Atomization of Aqueous Solutions, *Aerosol Science and Technology*, 46, 354–360, <https://doi.org/10.1080/02786826.2011.631614>, 2012.

Pasquier, J. T., Henneberger, J., Ramelli, F., Lauber, A., David, R. O., Wieder, J., Carlsen, T., Gierens, R., Maturilli, M., and Lohmann, U.: Conditions favorable for secondary ice production in Arctic mixed-phase clouds, *Atmos. Chem. Phys.*, 22, 15579–15601, <https://doi.org/10.5194/acp-22-15579-2022>, 2022.

1040 Persson, P. O. G., Fairall, C. W., Andreas, E. L., Guest, P. S., and Perovich, D. K.: Measurements near the Atmospheric Surface Flux Group tower at SHEBA: Near-surface conditions and surface energy budget, *J. Geophys. Res. Oceans*, 107, SHE 21-1-SHE 21-35, <https://doi.org/10.1029/2000JC000705>, 2002.

1045 Pikridas, M., Bezantakos, S., Moc'nik, G., Keleshis, C., Brechtel, F., Stavroulas, I., Demetriadis, G., Antoniou, P., Vouterakos, P., Argyrides, M., Liakakou, E., Drinovec, L., Marinou, E., Amiridis, V., Vrekoussis, M., Mihalopoulos, N., and Sciare, J.: On-flight intercomparison of three miniature aerosol absorption sensors using unmanned aerial systems (UASs), *Atmos. Meas. Tech.*, 23, 2019.

Pilz, C., Düsing, S., Wehner, B., Müller, T., Siebert, H., Voigtlander, J., and Lonardi, M.: CAMP: an instrumented platform for balloon-borne aerosol particle studies in the lower atmosphere, *Atmos. Meas. Tech.*, 15, 6889–6905, <https://doi.org/10.5194/amt-15-6889-2022>, 2022.

1050 Pitz, M., Cyrys, J., Karg, E., Wiedensohler, A., Wichmann, H.-E., and Heinrich, J.: Variability of Apparent Particle Density of an Urban Aerosol, *Environ. Sci. Technol.*, 37, 4336–4342, <https://doi.org/10.1021/es034322p>, 2003.

Porter, G. C. E., Sikora, S. N. F., Adams, M. P., Proske, U., Harrison, A. D., Tarn, M. D., Brooks, I. M., and Murray, B. J.: Resolving the size of ice-nucleating particles with a balloon deployable aerosol sampler: the SHARK, *Atmos. Meas. Tech.*, 13, 2905–2921, <https://doi.org/10.5194/amt-13-2905-2020>, 2020.

1055 Pratt, K. A. and Prather, K. A.: Aircraft measurements of vertical profiles of aerosol mixing states, *J. Geophys. Res. Atmos.*, 115, <https://doi.org/10.1029/2009JD013150>, 2010.

Samset, B. H., Myhre, G., Schulz, M., Balkanski, Y., Bauer, S., Berntsen, T. K., Bian, H., Bellouin, N., Diehl, T., Easter, R. C., Ghan, S. J., Iversen, T., Kinne, S., Kirkevåg, A., Lamarque, J.-F., Lin, G., Liu, X., Penner, J. E., Seland, Ø., Skeie, R. B., Stier, P., Takemura, T., Tsigaridis, K., and Zhang, K.: Black carbon vertical profiles strongly affect its radiative forcing uncertainty, *Atmos. Chem. Phys.*, 13, 2423–2434, <https://doi.org/10.5194/acp-13-2423-2013>, 2013.

1060 Sand, M., Samset, B. H., Balkanski, Y., Bauer, S., Bellouin, N., Berntsen, T. K., Bian, H., Chin, M., Diehl, T., Easter, R., Ghan, S. J., Iversen, T., Kirkevåg, A., Lamarque, J.-F., Lin, G., Liu, X., Luo, G., Myhre, G., Noije, T. van, Penner, J. E., Schulz, M., Seland, Ø., Skeie, R. B., Stier, P., Takemura, T., Tsigaridis, K., Yu, F., Zhang, K., and Zhang, H.: Aerosols at the poles: an AeroCom Phase II multi-model evaluation, *Atmos. Chem. Phys.*, 17, 12197–12218, <https://doi.org/10.5194/acp-17-12197-2017>, 2017.

1065 Schmale, J., Schneider, J., Jurkat, T., Voigt, C., Kalesse, H., Rautenhaus, M., Lichtenstern, M., Schlager, H., Ancellet, G., Arnold, F., Gerding, M., Mattis, I., Wendisch, M., and Borrmann, S.: Aerosol layers from the 2008 eruptions of Mount Okmok and Mount Kasatochi: In situ upper troposphere and lower stratosphere measurements of sulfate and organics over Europe, *J. Geophys. Res. Atmos.*, 115, <https://doi.org/10.1029/2009JD013628>, 2010.

1070 Schmale, J., Schneider, J., Ancellet, G., Quennehen, B., Stohl, A., Sodemann, H., Burkhart, J. F., Hamburger, T., Arnold, S. R., Schwarzenboeck, A., Borrmann, S., and Law, K. S.: Source identification and airborne chemical characterisation of aerosol pollution from long-range transport over Greenland during POLARCAT summer campaign 2008, *Atmos. Chem. Phys.*, 11, 10097–10123, <https://doi.org/10.5194/acp-11-10097-2011>, 2011.

1075 Schmale, J., Henning, S., Decesari, S., Henzing, B., Keskinen, H., Sellegri, K., Ovadnevaite, J., Pöhlker, M. L., Brito, J., Bougiatioti, A., Kristensson, A., Kalivitis, N., Stavroulas, I., Carbone, S., Jefferson, A., Park, M., Schlag, P., Iwamoto, Y., Aalto, P., Äijälä, M., Bukowiecki, N., Ehn, M., Frank, G., Fröhlich, R., Frumau, A., Herrmann, E., Herrmann, H., Holzinger, R., Kos, G., Kulmala, M., Mihalopoulos, N., Nenes, A., O'Dowd, C., Petäjä, T., Picard, D., Pöhlker, C., Pöschl, U., Poulain, L., Prévôt, A. S. H., Swietlicki, E., Andreae, M. O., Artaxo, P., Wiedensohler, A., Ogren, J., Matsuki, A., Yum, S. S., Stratmann, F., Baltensperger, U., and Gysel, M.: Long-term cloud condensation nuclei number concentration, particle number size distribution and chemical composition measurements at regionally representative observatories, *Atmos. Chem. Phys.*, 29, 2018.

Seinfeld, J. H. and Pandis, S. N.: Atmospheric chemistry and physics: from air pollution to climate change, John Wiley&Sons., Hoboken, USA, 1326 pp., 2016.

1080 Simpson, W., Law, K., Schmale, J., Pratt, K., Arnold, S., Mao, J., Alexander, B., Anenberg, S., Baklanov, A., Bell, D., Brown, S., Creamean, J., de Boer, G., DeCarlo, P., Descari, S., Elleman, R., Flynn, J., Fochesatto, J., Ganzenfeld, L., Gilmour, I., Griffin, R., Järvi, L., Kaspari, S., Konstantinov, P., Murphy, J., Petäjä, T., Pye, H., Raut, J.-C., Roberts, T., Shiraiwa, M., Stutz, J., Thomas, J., Thornton, J., Wagstrom, K., Weber, R., Webley, P., and Williams, B.: Alaskan Layered Pollution And Chemical Analysis (ALPACA) White Paper, 84, 2019.

1085 Spanu, A., Dollner, M., Gasteiger, J., Bui, T. P., and Weinzierl, B.: Flow-induced errors in airborne in situ measurements of aerosols and clouds, *Atmos. Meas. Tech.*, 13, 1963–1987, <https://doi.org/10.5194/amt-13-1963-2020>, 2020.

Springston, S., Chand, D., Ermold, B., Shilling, J., and Flynn, C.: Ozone Monitor (OZONE) Instrument Handbook, <https://doi.org/10.2172/1246164>, 2020.

1090 Stolzenburg, M. R. and McMurry, P. H.: An Ultrafine Aerosol Condensation Nucleus Counter, *Aerosol Science and Technology*, 14, 48–65, <https://doi.org/10.1080/02786829108959470>, 1991.

1095 Thorsen, T. J. and Fu, Q.: CALIPSO-inferred aerosol direct radiative effects: Bias estimates using ground-based Raman lidars, *J. Geophys. Res. Atmos.*, 120, 12,209–12,220, <https://doi.org/10.1002/2015JD024095>, 2015.

Travis, B., Dubey, M., and Sauer, J.: Neural networks to locate and quantify fugitive natural gas leaks for a MIR detection system, *Atmospheric Environment: X*, 8, 100092, <https://doi.org/10.1016/j.aeaoa.2020.100092>, 2020.

1100 von der Weiden, S.-L., Drewnick, F., and Borrmann, S.: Particle Loss Calculator – a new software tool for the assessment of the performance of aerosol inlet systems, *Atmos. Meas. Tech.*, 2, 479–494, <https://doi.org/10.5194/amt-2-479-2009>, 2009.

Willis, R. D. and Blanchard, F. T.: Guidelines for the Application of SEM/EDX Analytical Techniques to Particulate Matter Samples, 2002.

World Meteorological Organization: WMO/GAW Aerosol Measurement Procedures, Guidelines and Recommendations, 2016.

1105

1110



Figure 1: Picture of the MoMuCAMS payload attached to the helikite. Two aluminum bars connected directly to the helikite's structure ensure stability of the payload. Two additional cargo straps provide additional safety for the payload attachment. The system remains very stable, even at winds above 15 m s^{-1} .

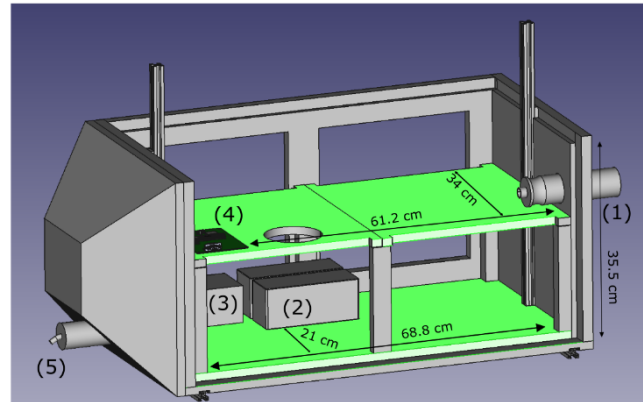
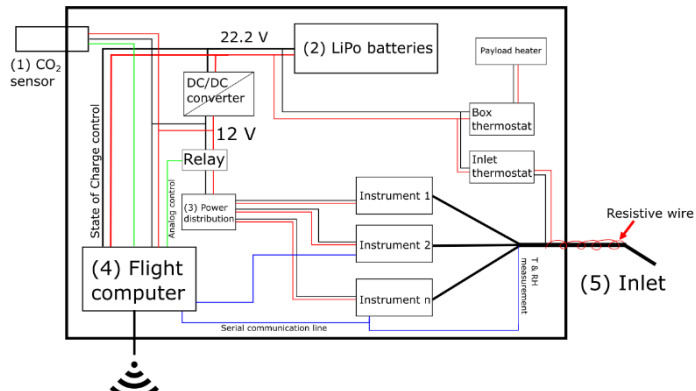


Figure 2: (a) Schematic of MoMuCAMS design. Black and red paths represent power wires. Blue and green lines represent serial and analog communication connections for communication between different instruments/components and the flight computer. The setup is flexible and can accommodate different aerosol and trace gas instruments, thus the layout of instruments is only illustrative. (b) 3D drawing of MoMuCAMS enclosure without side panels and top cover. Green surfaces represent available space for instrumentation. Numbered elements are introduced on panel (a).

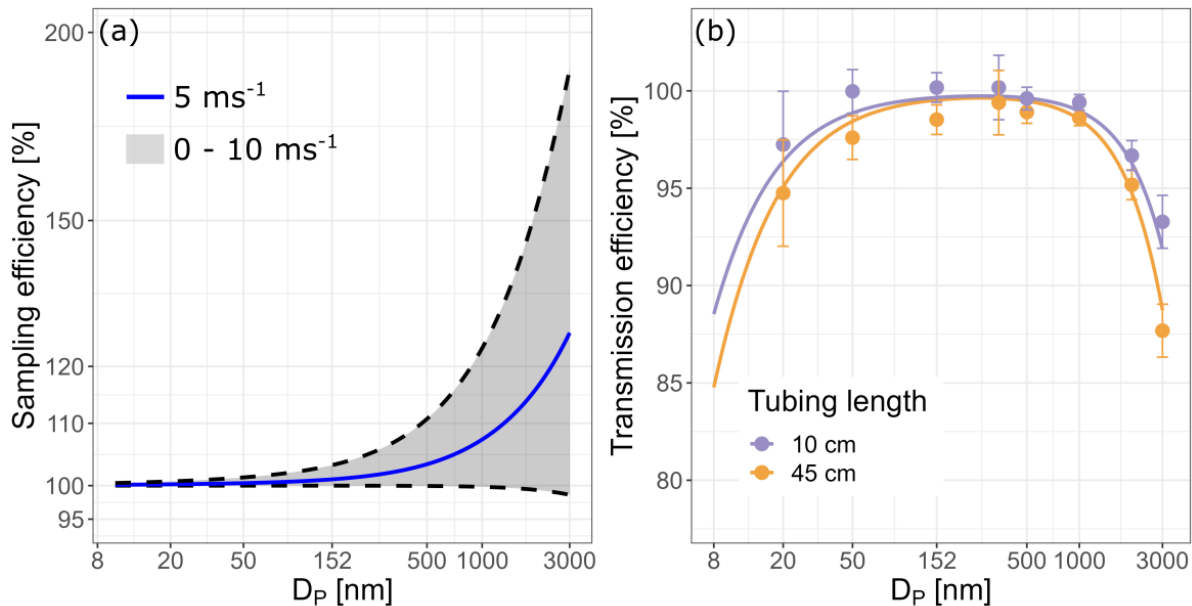


Figure 3: a) Inlet sampling efficiency at 1.72 lpm sampling flow. The shaded area represents wind speeds between 0 and 10 m s^{-1} . The blue line represents the sampling efficiency at 5 ms^{-1} . b) Inlet transmission results from experimental tests and the PLC. Each dot represents a 5-minute average of transmission efficiency measurements and the error bars represent the standard deviation. The two lines are results obtained from the PLC. Colors indicate the length of the black tubing connecting the end of the stainless steel inlet to the CPC and represent the range of line lengths inside MoMuCAMS.

1145

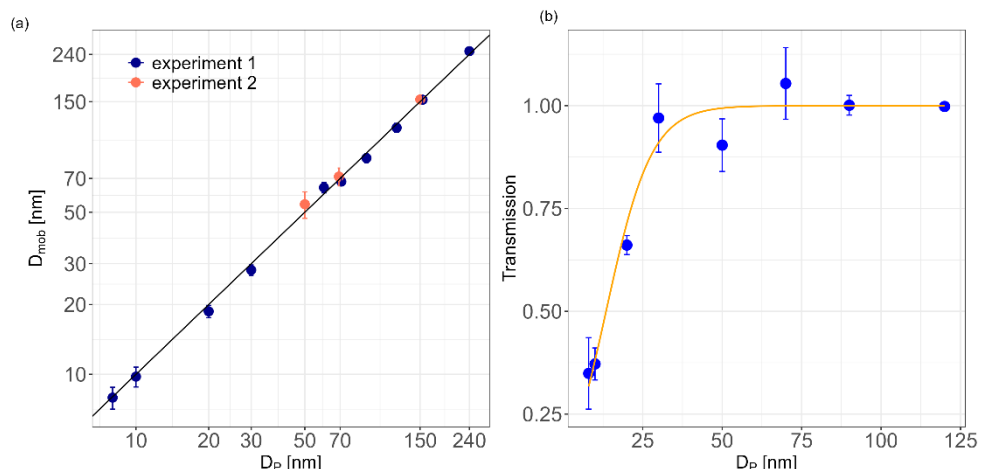
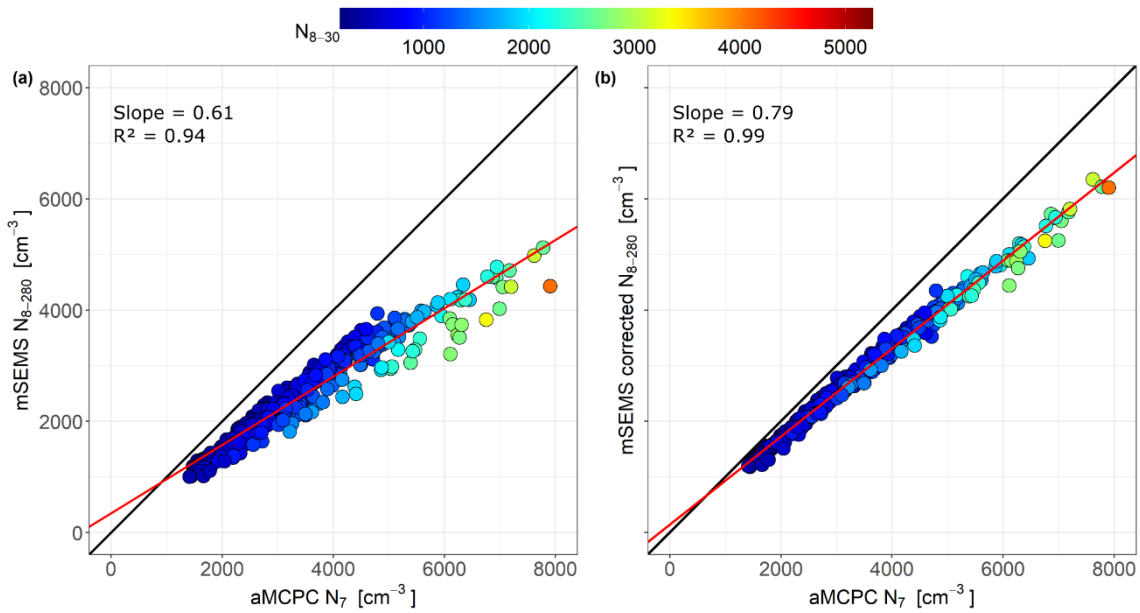
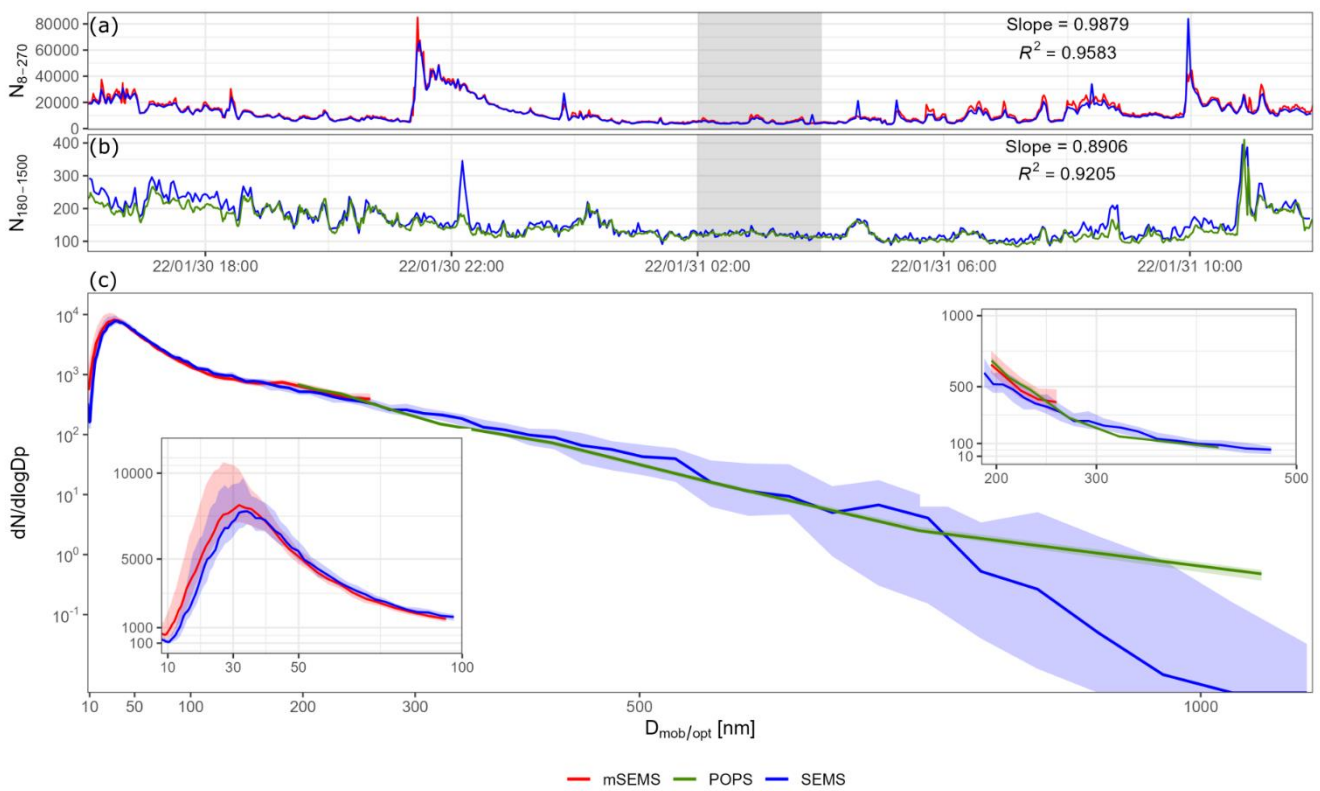


Figure 4: a) Measured particle mobility diameter (D_{mob}) from a lognormal fit of the measured PNNSD from the mSEMS against the diameter of reference PSL or impurities from nebulized MilliQ water mean diameter. The black line represents equal diameters of PSL reference particles and measured D_{mob} . The experiment was conducted on two separate occasions (experiment 1 and 2). Uncertainty Error bars indicate of the main mode is defined by one the standard deviation of the lognormal distribution fitted to the mSEMS measurement. b) Particle transmission through the DMA. Error bars indicate the standard deviation of the period of comparison (15 min). The orange curve represents the best fit of the theoretical transmission function (Eq. 1).

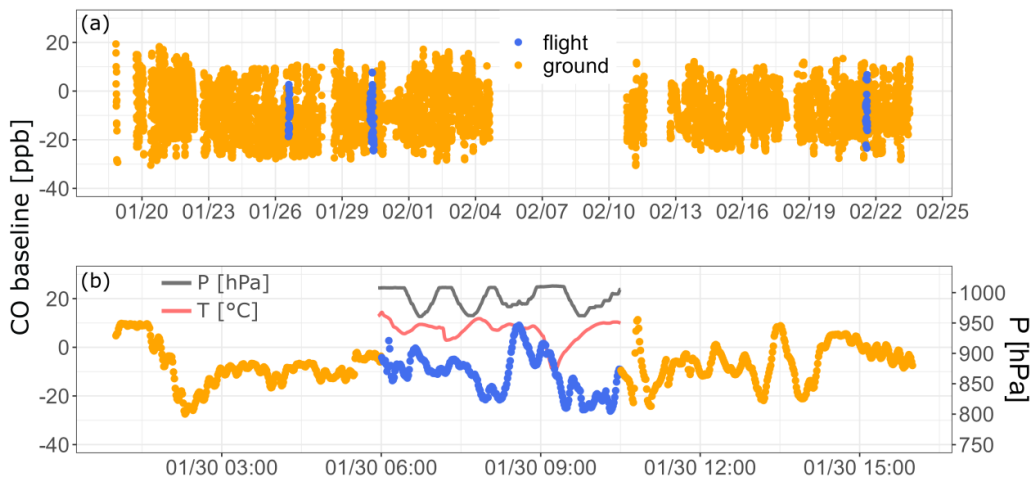
1150



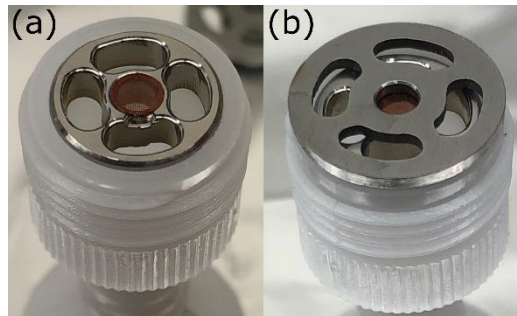
1155
Figure 5: Scatter plots of 10-min averaged particle number concentration. Panel (a) shows concentration from the aMCPC (x-axis) against the integrated measured concentration from the mSEMS (y-axis). Panel (b) shows the same but with corrected mSEMS data. The color scale indicates the total concentration of particles between 8 and 30 nm.



1160
Figure 6: Comparison of the mSEMS, SEMS and POPS between January 30 and 31, 2022. Measurements were performed at the University of Alaska farm field in Fairbanks, USA (64°51'12"N / 147°51'34" W). a) Timeseries of particle number concentration from 8 to 280 nm (N_{8-280}) from mSEMS (red) and SEMS (blue). b) Timeseries of particle number concentration from 180 to 1500 nm ($N_{180-1500}$) from POPS (green) and SEMS (blue). c) Particle number size distribution measured from 02:00 and 04:00 on January 31 (shaded grey area in (a) and (b)).

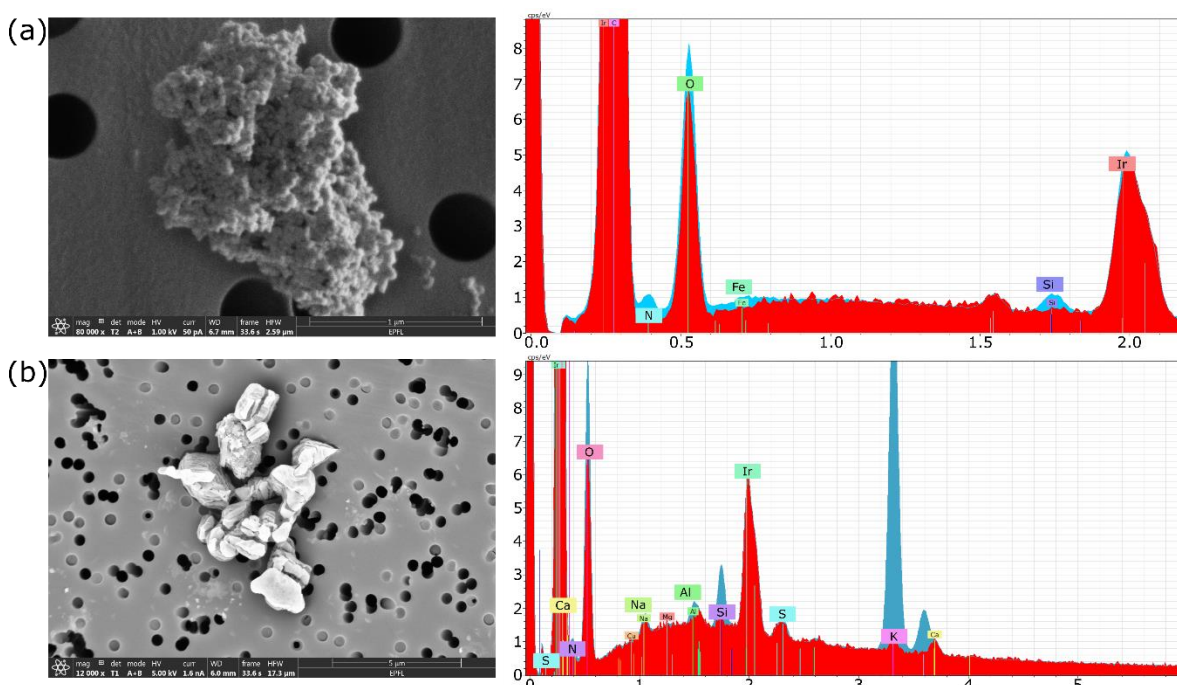


1170 Figure 7: a) CO baseline measurements of MIRA Pico during the ALPACA campaign from January 18 to February 24, 2022. Blue dots indicate measurements of the baseline during flights. b) Subset of baselinezero measurements before, during and after a flight on January 30, 2022. The black and red lines represent the barometric pressure (right axis) and temperature inside the MoMuCAMS enclosurebox (left axis), respectively.



1175

Figure 8: a) TEM grid placed on custom-made grid holder. b) TEM grid with covering plate placed on top.



1180 Figure 10: SEM/EDX of two particles collected during airborne sampling on a) September 28 and b) October 7, 2021. Red spectra represent the EDX signal collected when pointing the electron beam only on the filter substrate which serves as a type of blank. Blue spectra indicate the EDX signal from the particle. (The SEM pictures were obtained in collaboration with Emad Oveisi, EPFL)

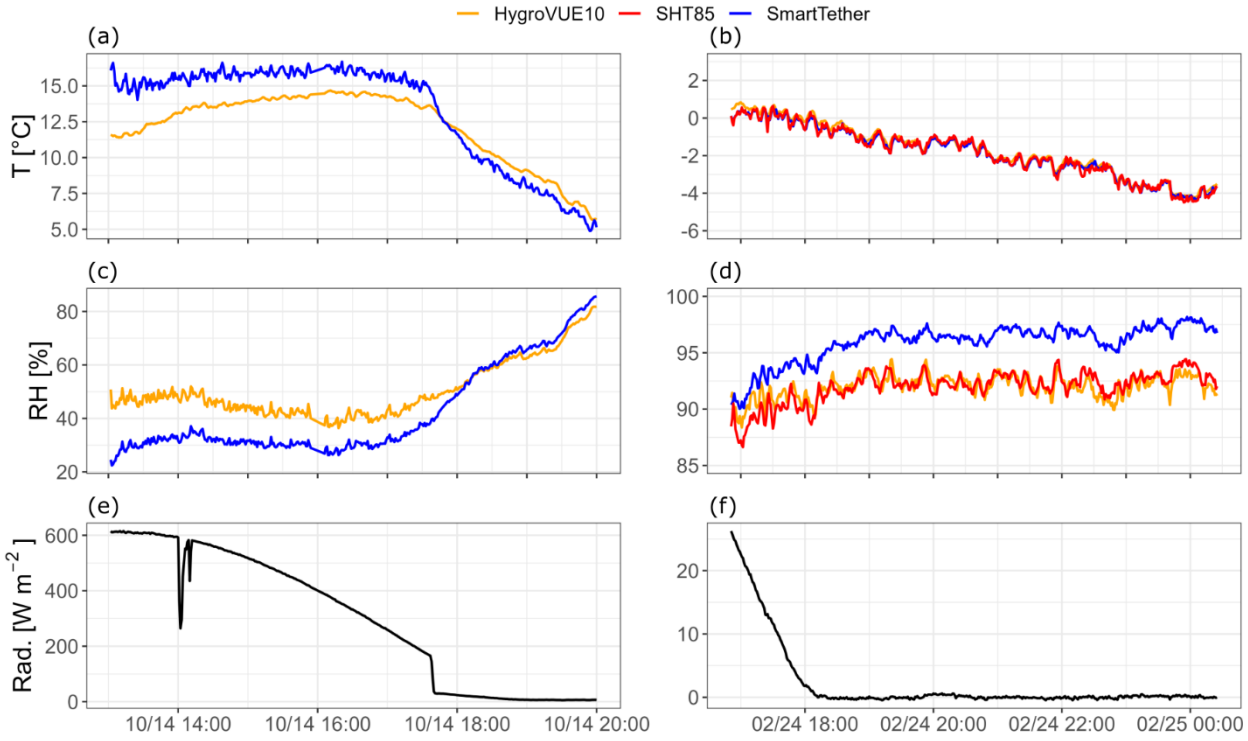


Figure 9: Timeseries of temperature (T) (panels a and b), relative humidity (RH) (panels c and d) for the SmartTether (blue line), SHT80 sensor (red line) and HygroVUE10 reference sensor (orange line) during two comparison experiments (left and right columns). Bottom panels (e and f) indicated incoming shortwave radiation (Rad.) in black. Time is indicated in local time for both panels, CEST (left) and AKST (right). The first comparison was performed in Brigerbad, CH (46°18'00"N / 7°55'16"E) and the second in Fairbanks, USA (64°51'12"N / 147°51'34"W).

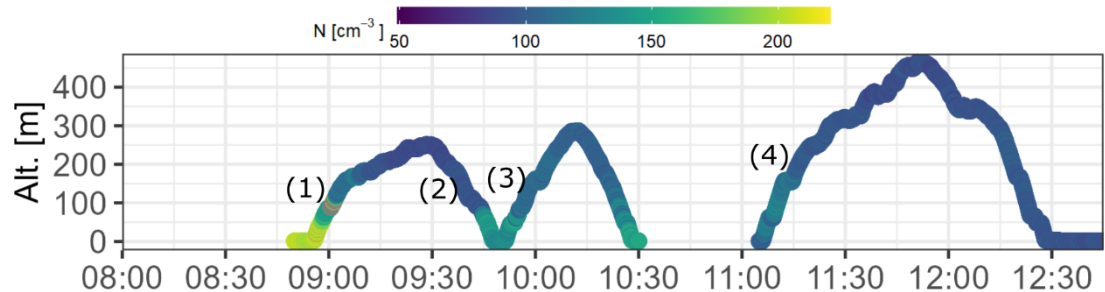
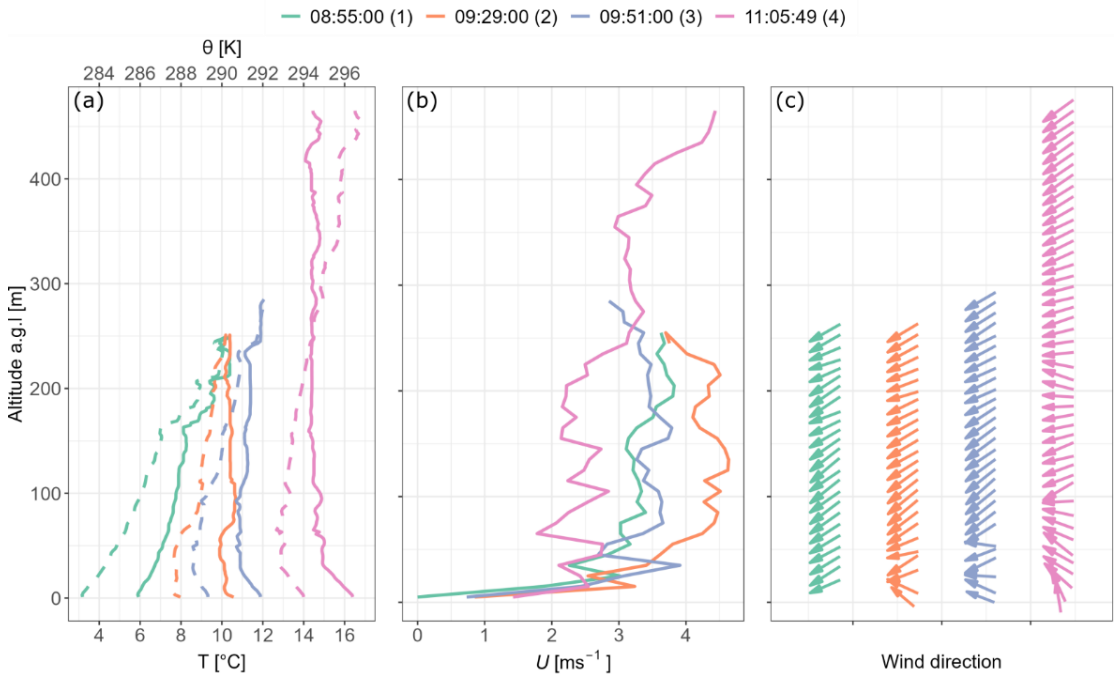
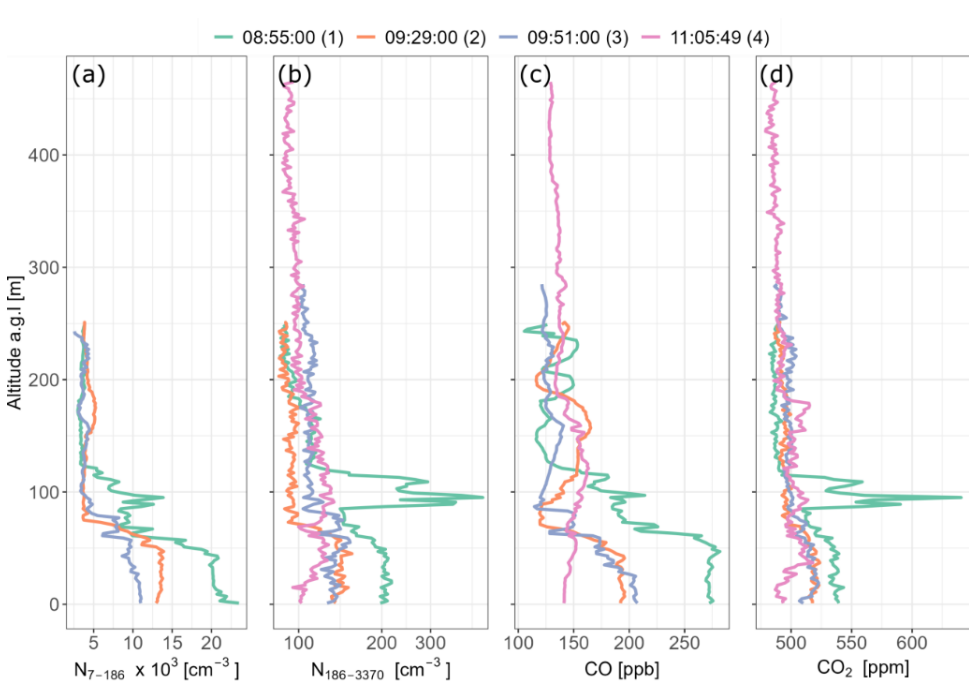


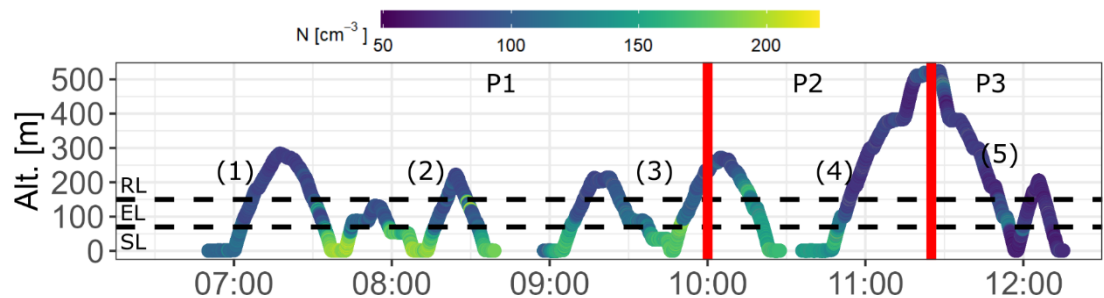
Figure 10: Time-series of balloon altitude above ground level [m] on October 1, 2022, of (a) temperature (T), net radiation (NR) and wind speed (U) and direction (arrows) measured at the surface, (b) measured particle size distribution at the surface, (c) integrated total concentration (black dots) at the surface. Blue diamonds indicate the measured particle concentration (N₇) onboard MoMuCAMS when the helikite was at the surface, (d) balloon altitude above ground level [m]. The color scale indicates number particle concentration (>186 - 3370 nm). Numbers in brackets indicate the different profiles shown in Fig. 11 and 12. Location: 46°18'00"N / 7°55'16"E.



1205 | **Figure 11:** Vertical profiles of (a) temperature (T - full lines) and potential temperature (θ - dashed lines), (b) wind speed (U) and (c) wind direction. Temperature is displayed at a 2-meter spatial resolution, corresponding on average to ten data points, whereas wind is displayed at a 10-meter resolution, for an average of 25 data points.



1210 | **Figure 12:** Vertical profiles of (a) particle number concentrations in the size range of 7 to 186 nm, (b) particle number concentration in size range of 186 to 3370 nm, (c) CO mixing ratio, and (d) CO₂ mixing ratio. Data are displayed at a 2-meter spatial resolution, corresponding on average to ten data points. The displayed time on panel a) indicates the beginning of each profile.



1220 **Figure 13:** Timeseries on October 14, 2022 of (a) temperature (T), net radiation (NR) and wind speed (U) and direction (arrows) measured at the surface, (b) measured particle size distribution at the surface, (c) integrated total concentration at the surface and (d) balloon altitude above ground level [m]. The color scale indicates particle number concentration (>186nm). Numbers in brackets indicate the different profiles shown in Fig. 14. P1, P2 and P3 refer to the three time periods discussed in Fig. 15.

1225

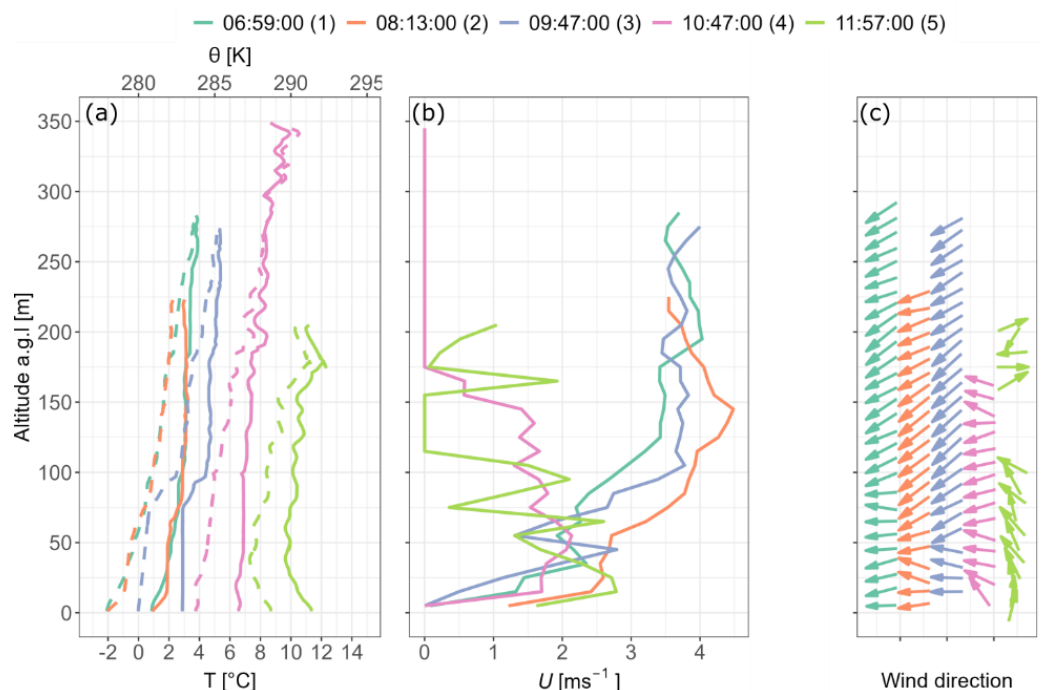
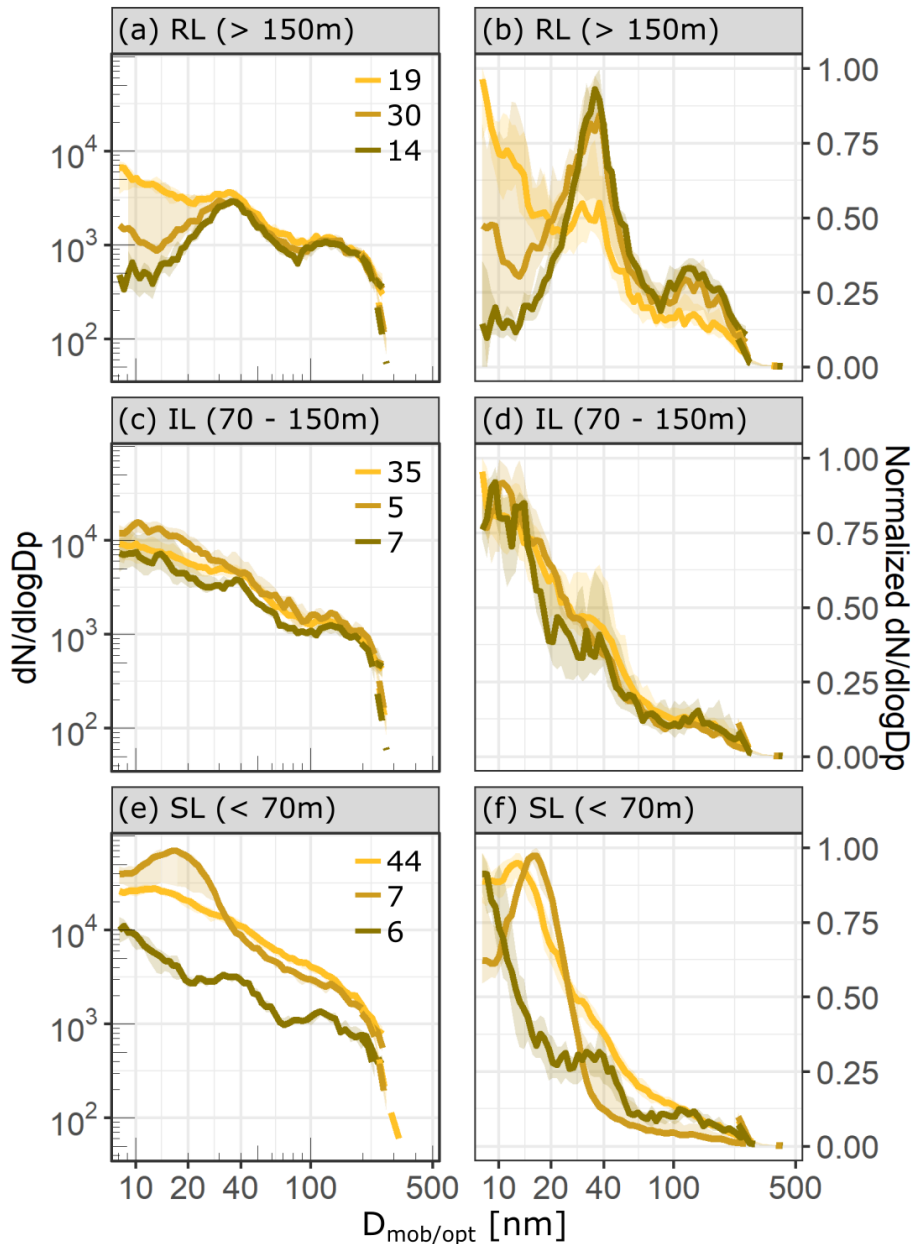


Figure 14: Vertical profiles of (a) temperature (T) (T - full lines) and potential temperature (θ - dashed lines), (b) wind speed (U) and (c) wind direction. Temperature is displayed at a 2-meter spatial resolution, corresponding on average to ten data points, whereas wind is displayed at a 10-meter resolution, for an average of 25 data points.

— 07:30 - 09:59 (P1) — 10:00 - 11:15 (P2) — 11:35 - 12:15 (P3)



1230 | Figure 15: Evolution of particle size distributions between 8 and 500 nm in the residual layers (>150 m, a and b), intermediate layer (70 – 150m, b and e) and surface layer (0 – 70m, e and f). Solid lines indicate the median PNNSD measured by the mSEMS while shadings represent the interquartile range. Dashed lines represent the POPSSD measured by the POPS. Colors indicate the three periods P1, P2 and P3. Left panels (a, c and e) represent the $dN/d\log D_p$ size distribution. Numbers in the upper right corners indicate the number of scans collected per layer and period. Right panels (b, d and f) show normalized distributions where each $dN/d\log D_p$ value of a scan was divided by the maximum $dN/d\log D_p$ measured for the respective scan.

1235

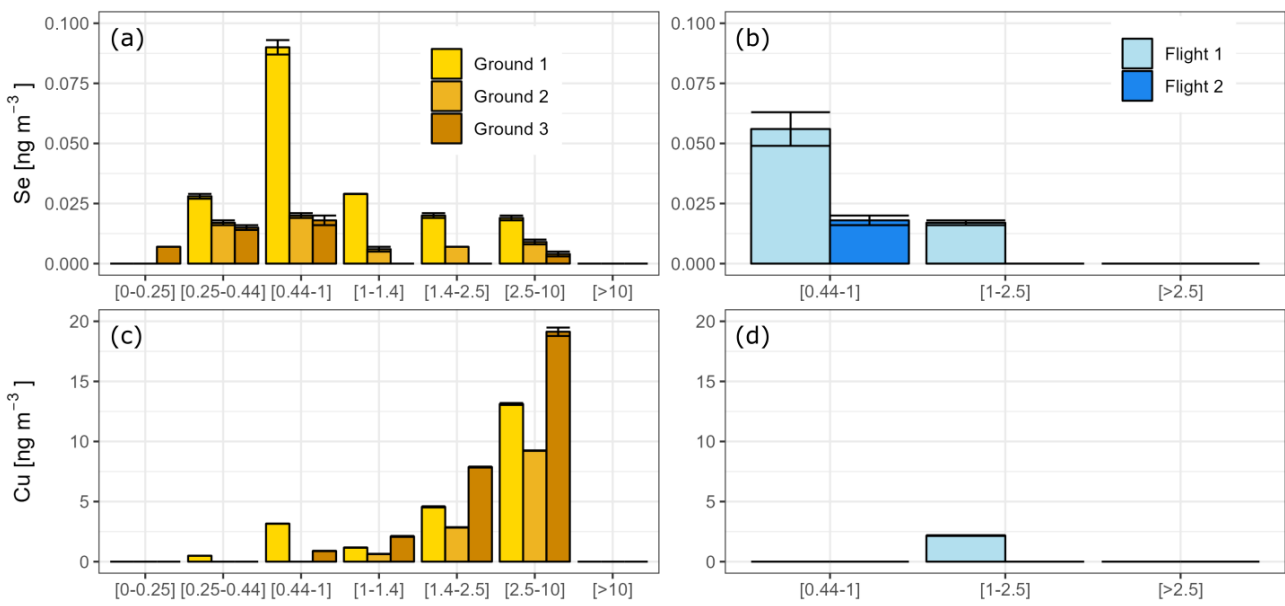


Figure 16: Size segregated measured concentrations by ICP-MS/MS of selenium (Se) at the surface (a) and during flight (b) and of copper (Cu) at the surface (c) and during flight (d). The absence of a colored bar indicates that measured values were below the detection limit.

1240

Table 1: List of instruments available on MoMuCAMS

Measurement / Analysis performed	Instrument	Manufacturer	Weight (kg)	Sampling flow (lpm)	Time resolution	Mode of operation	Uncertainty
<u>Aerosols</u>							
Particle size distribution (186 – 3370 nm)	Portable Optical Particle Spectrometer (POPS)	Handix Scientific	0.86	0.18	1s	16 size bins	cf. Sect. 3.4
<u></u>							
Particle size distribution (8 – 300 nm)	Miniaturized Scanning Electrical Mobility Spectrometer (mSEMS)	Brechtel Manufacturing Inc	1.58	0.36 (0.1 – 0.76)*	1s	60 size bins / 1 sec per bin	cf. Sect. 3.3
Particle number concentration (7 – 2000 nm)	Advanced Mixing Condensation Particle Counter (aMCPC)		1.7	0.36	1s	=	< 5%
<u></u>							
Aerosol light absorption at 450, 525 and 624 nm	Single Channel Tricolor Absorption Photometer (STAP)		0.73	1.0 (0.5 – 1.7)*	1 min	=	$\pm 0.2 \text{ Mm}^{-1}$
<u></u>							
Microscopic analysis (SEM-EDX, TEM-EDX**)	8-channel filter sampler (FILT)		0.7	1.5 (0.5 – 3.3)*	Adjustable, depends on mass	e.g., 1 hour sampling per filter at	=

							<u>concentrations, typically hours</u>	<u>constant altitude</u>
<u>Chemical analysis (IC, ICP-MS***)</u>	<u>HFI stage impactor</u> <u>Model 131A</u>	<u>TSI</u>	<u>2.0</u>	<u>100</u>				<u>-</u>
<u>Trace gases</u>								
<u>CO₂ mixing ratio</u>	<u>CO₂ monitor</u> <u>GMP343</u>	<u>Vaisala</u>	<u>0.4</u>	<u>(diffusion)</u>	<u>2s</u>		<u>-</u>	<u>± 3 ppm + 1% of reading</u>
<u>O₃ mixing ratio</u>	<u>O₃ monitor</u> <u>Model 205</u>	<u>2BTech</u>	<u>1.94</u>	<u>1.8</u>	<u>2s</u>		<u>-</u>	<u>Greater of 1 ppb or 2% of reading</u>
<u>CO and N₂O mixing ratio</u>	<u>MIRA Pico</u>	<u>Aeris Technologies</u>	<u>2.7</u>		<u>1s / 1 min</u>	<u>manual mode / differential mode</u>		<u>CO: <1 ppb N₂O: <1 ppb</u>
<u>Meteorology</u>								
<u>T, RH, P, Wind speed and direction, lat, lon</u>	<u>SmartTether</u>	<u>Anasphere</u>	<u>0.150</u>		<u>2s</u>		<u>-</u>	<u>cf. Table 3</u>
<u>T and RH</u>	<u>SHT85</u>	<u>Sensirion</u>		<u>-</u>	<u>1s</u>		<u>-</u>	<u>T: 0.1°C RH: 1.5%</u>

1245 *Values in brackets represent the range of possible sampling flows, while the single value indicates the typical flow set during operations.

**SEM-EDX = Scanning electron microscopy with energy dispersive x-ray analysis, TEM-EDX = Transmission electron microscopy with energy dispersive x-ray analysis (the analysis is done in laboratory after the flights).

1250 ***IC = Ion chromatography, ICP-MS = Inductively coupled plasma tandem mass spectrometry (the analysis is done in laboratory after the flights).

Table 2: Summary table of background concentration values (in ng) for copper (Cu) and selenium (Se) extracted from 7 blanks (4 regular blanks and 3 field blanks) digested and measured by inductively coupled plasma tandem mass spectrometry analysis (ICP-MS/MS). The last column indicates the obtained detection limit calculated as the mean plus three standard deviations.

Element	Mean	Standard deviation	Detection limit
	(ng)	(ng)	(ng)
Cu	8	5	22
Se	0.05	0.02	0.12

1255 _____

Table 2 Results of mSEMS performance. D_{mob} indicates the peak of the fitted lognormal distribution for the respective particle diameter (D_p). σ represents the standard deviation of fitted distribution and |Δ_{D_{mob}-D_p}| represents the absolute deviation in percent between D_{mob} and D_p.

<u>D_p [nm]</u>	<u>8</u>	<u>10</u>	<u>20</u>	<u>30</u>	<u>51</u>	<u>60</u>	<u>70</u>	<u>90</u>	<u>120</u>	<u>152</u>	<u>240</u>
<u>D_{mob} [nm]</u>	<u>7.93</u>	<u>9.77</u>	<u>18.7</u>	<u>28.2</u>	<u>54.1</u>	<u>63.9</u>	<u>67.8</u> [71.3]	<u>85.7</u>	<u>115.8</u>	<u>152.9</u> [153.3]	<u>247.7</u>
<u>σ [nm]</u>	<u>0.86</u>	<u>0.96</u>	<u>1.14</u>	<u>1.46</u>	<u>7.03</u>	<u>3.3</u>	<u>2.8</u> [6.3]	<u>3.92</u>	<u>5.14</u>	<u>6.24</u> [4.9]	<u>8.7</u>

$ \Delta D_{mob-Dp} [\%]$	0.9	2.3	6.6	6.1	6.1	6.5	3.1 [1.86]	4.8	3.5	0.6 [0.86]	3.2
----------------------------	-----	-----	-----	-----	-----	-----	---------------	-----	-----	---------------	-----

1265

Table 3: Meteorological parameters measured with SmartTether.

Measurement	Sensor (model, manufacturer)	Unit	Resolution	Accuracy	Range
Pressure (P)	MS5540C, Intersema	hPa	0.1	± 0.5	0 to 1100
Temperature (T)	DS18B20, Maxim Integrated	° C	0.125	± 0.5	-55 to +125
Relative humidity (RH)	HIH9131, Honeywell	%	0.1	± 3	0 to 100
Wind speed (WS)	-	$m s^{-1}$	0.1	± 0.1	0 to 59
Wind direction (WD)	-	°	1	± 2	0 to 359

1270

Table 4: Measured variables during flights

	01/10	14/10
Particle Number Concentration (>7nm)	*	*
Particle size distribution (8-270 nm)	*	
Particle size distribution (186-3300 nm)	*	*
CO	*	
CO₂	*	*
O₃	*	
Meteorological parameters (T, RH, P, WS, WD)	*	*

1275 *aMCPC was removed for the 3rd profile.**Table 4: Summary of ground and flight filter sampling.**

Date	Mean sampling altitude above ground [m]	Altitude standard deviation [m]	Sampling time [h]	MOUDI sampled volume [m ³]	Number of filters collected for SEM	Number of filters collected for TEM

Flight 1	09/28	279	59	5	30.2	3	2
Flight 2	10/07	434	47	4.85	28.9	3	3
Ground	09/27	0.6	-	17.9	107.4	-	-
1							
Ground	10/06	0.6	-	17	102.1	-	-
2							
Ground	10/07	0.6	-	12.7	76.1	-	-
3							